

AD 727618

MICROSTRUCTURE STUDIES OF REFRACTORY

POLYCRYSTALLINE OXIDES

SUMMARY REPORT

1 April 1970 to 1 February 1971

Contract N00019-70-C-0171

AVSD-0192-71-CR

Prepared for

U.S. Naval Air Systems
Washington 25, D.C.

APPROVED FOR PUBLIC RELEASE;
DISTRIBUTION UNLIMITED

Prepared by

W.H. Rhodes
R.M. Cannon

Reproduced by
NATIONAL TECHNICAL
INFORMATION SERVICE
Springfield, Va. 22151

AVCO CORPORATION
Systems Division
Lowell, Massachusetts 01851

DDC
RECEIVED
AUG 4 1971
C

Unclassified

Security Classification

DOCUMENT CONTROL DATA - R&D		
(Security classification of title, body of abstract and indexing annotation must be entered when the overall report is classified)		
1. ORIGINATING ACTIVITY (Corporate author)		2a. REPORT SECURITY CLASSIFICATION
Avco Corporation Systems Division Lowell, Massachusetts 01851		Unclassified
		2b. GROUP
3. REPORT TITLE		
Microstructure Studies of Refractory Polycrystalline Oxides		
4. DESCRIPTIVE NOTES (Type of report and inclusive dates)		
Summary Report, 1 April 1970 to 1 February 1971		
5. AUTHOR(S) (Last name, first name, initial)		
William H. Rhodes Rowland M. Cannon		
6. REPORT DATE	7a. TOTAL NO. OF PAGES	7b. NO. OF REFS
1 April 1970 to 1 February 1971	58	38
8a. CONTRACT OR GRANT NO.	8b. ORIGINATOR'S REPORT NUMBER(S)	
N00019-70-C-0171	AVSD-0192-71-CR	
a. PROJECT NO.		
c.	9b. OTHER REPORT NO(S) (Any other numbers that may be assigned this report)	
d.		
10. AVAILABILITY/LIMITATION NOTICES		
This document is subjected to special export controls and each transmittal to foreign governments or foreign nationals may be made only with the prior approval of the Commander, Naval Air Systems Command.		
11. SUPPLEMENTARY NOTES		12. SPONSORING MILITARY ACTIVITY
		Naval Air Systems Command Washington, D.C.
13. ABSTRACT		
<p>This study was concerned with the interaction between microstructure and chemistry in polycrystalline MgO and Al₂O₃ and several facets of mechanical properties. Further, the press forging of Al₂O₃ hemispheres was undertaken. Earlier work had shown that press forging developed unique optical and mechanical properties. A direct comparison of deformation in the high purity Al₂O₃ and less pure Al₂O₃ + 1/4% MgO with a nearly identical grain size and porosity demonstrated that the deformation rates were very close within a limited temperature regime. Several pieces of evidence to include a higher strain rate sensitivity which decreased with increasing temperature led to the conclusion that deformation in high purity fine-grained Al₂O₃ shifts from grain boundary diffusion to a strong component of grain boundary sliding at higher temperatures. The differences between the grades of Al₂O₃ were attributed to the influence of impurities and dopants on grain-to-grain bond strength. Stress corrosion studies on two grades of hot pressed MgO and one grade of sintered MgO demonstrated marked differences among the grades and further differences in test environments known to react chemically and/or to influence dislocation mobilities in MgO. The corrosion curves as well as fractographic studies support the view that stress corrosion in H₂O is dominated by stress enhanced chemical corrosion which is strongly dependent on grain boundary impurity phases. Further, in the absence of H₂O a mechanical stress corrosion model may dominate as the static fatigue limit was influenced by organic media known to affect dislocation mobility. The hemisphere press forging study was preliminary and mainly concerned with preform preparation.</p>		

DD FORM 1473

Unclassified

(cont'd)

Security Classification

14 KEY WORDS	LINK A		LINK B		LINK C	
	ROLE	WT	ROLE	WT	ROLE	WT
Alumina Magnesia Hot Pressing Press Forging Mechanical Properties Stress Corrosion Plastic Deformation High Purity						

INSTRUCTIONS

1. **ORIGINATING ACTIVITY:** Enter the name and address of the contractor, subcontractor, grantee, Department of Defense activity or other organization (*corporate author*) issuing the report.

2a. **REPORT SECURITY CLASSIFICATION:** Enter the overall security classification of the report. Indicate whether "Restricted Data" is included. Marking is to be in accordance with appropriate security regulations.

2b. **GROUP:** Automatic downgrading is specified in DoD Directive 5200.10 and Armed Forces Industrial Manual. Enter the group number. Also, when applicable, show that optional markings have been used for Group 3 and Group 4 as authorized.

3. **REPORT TITLE:** Enter the complete report title in all capital letters. Titles in all cases should be unclassified. If a meaningful title cannot be selected without classification, show title classification in all capitals in parenthesis immediately following the title.

4. **DESCRIPTIVE NOTES:** If appropriate, enter the type of report, e.g., interim, progress, summary, annual, or final. Give the inclusive dates when a specific reporting period is covered.

5. **AUTHOR(S):** Enter the name(s) of author(s) as shown on or in the report. Enter last name, first name, middle initial. If military, show rank and branch of service. The name of the principal author is an absolute minimum requirement.

6. **REPORT DATE:** Enter the date of the report as day, month, year; or month, year. If more than one date appears on the report, use date of publication.

7a. **TOTAL NUMBER OF PAGES:** The total page count should follow normal pagination procedures, i.e., enter the number of pages containing information.

7b. **NUMBER OF REFERENCES:** Enter the total number of references cited in the report.

8a. **CONTRACT OR GRANT NUMBER:** If appropriate, enter the applicable number of the contract or grant under which the report was written.

8b, 8c, & 8d. **PROJECT NUMBER:** Enter the appropriate military department identification, such as project number, subproject number, system numbers, task number, etc.

9a. **ORIGINATOR'S REPORT NUMBER(S):** Enter the official report number by which the document will be identified and controlled by the originating activity. This number must be unique to this report.

9b. **OTHER REPORT NUMBER(S):** If the report has been assigned any other report numbers (*either by the originator or by the sponsor*), also enter this number(s).

10. **AVAILABILITY/LIMITATION NOTICES:** Enter any limitations on further dissemination of the report, other than those imposed by security classification, using standard statements such as:

- (1) "Qualified requesters may obtain copies of this report from DDC."
- (2) "Foreign announcement and dissemination of this report by DDC is not authorized."
- (3) "U. S. Government agencies may obtain copies of this report directly from DDC. Other qualified DDC users shall request through _____."
- (4) "U. S. military agencies may obtain copies of this report directly from DDC. Other qualified users shall request through _____."
- (5) "All distribution of this report is controlled. Qualified DDC users shall request through _____."

If the report has been furnished to the Office of Technical Services, Department of Commerce, for sale to the public, indicate this fact and enter the price, if known.

11. **SUPPLEMENTARY NOTES:** Use for additional explanatory notes.

12. **SPONSORING MILITARY ACTIVITY:** Enter the name of the departmental project office or laboratory sponsoring (*paying for*) the research and development. Include address.

13. **ABSTRACT:** Enter an abstract giving a brief and factual summary of the document indicative of the report, even though it may also appear elsewhere in the body of the technical report. If additional space is required, a continuation sheet shall be attached.

It is highly desirable that the abstract of classified reports be unclassified. Each paragraph of the abstract shall end with an indication of the military security classification of the information in the paragraph, represented as (TS), (S), (C), or (U).

There is no limitation on the length of the abstract. However, the suggested length is from 150 to 225 words.

14. **KEY WORDS:** Key words are technically meaningful terms or short phrases that characterize a report and may be used as index entries for cataloging the report. Key words must be selected so that no security classification is required. Identifiers, such as equipment model designation, trade name, military project code name, geographic location, may be used as key words but will be followed by an indication of technical context. The assignment of links, rules, and weights is optional.

Unclassified

Security Classification

DOCUMENT CONTROL DATA - R&D		
<small>(Security classification of title, body of abstract and indexing annotation must be entered when the overall report is classified)</small>		
1 ORIGINATING ACTIVITY (Corporate author) Avco Corporation Systems Division Lowell, Massachusetts 01851		2a REPORT SECURITY CLASSIFICATION Unclassified
		2b GROUP
3 REPORT TITLE Microstructure Studies of Refractory Polycrystalline Oxides		
4 DESCRIPTIVE NOTES (Type of report and inclusive dates) Summary Report, 1 April 1970 to 1 February 1971		
5 AUTHOR(S) (Last name, first name, initial) William H. Rhodes Rowland M. Cannon		
6 REPORT DATE 1 April 1970 to 1 February 1971	7a. TOTAL NO. OF PAGES 58	7b. NO. OF REFS 38
8a. CONTRACT OR GRANT NO.	8a. ORIGINATOR'S REPORT NUMBER(S) AVSD-0192-71-CR	
b. PROJECT NO.		
c.	8b. OTHER REPORT NO(S) (Any other numbers that may be assigned this report)	
d.		
10. AVAILABILITY/LIMITATION NOTICES APPROVED FOR PUBLIC RELEASE; DISTRIBUTION UNLIMITED		
11. SUPPLEMENTARY NOTES		12. SPONSORING MILITARY ACTIVITY
13. ABSTRACT (Concluded) die design, lubrication and establishing process limits. The central zone of several hemispheres were crack-free and translucent with limited edge tearing. Also, a basal crystallographic texture parallel to the surface was developed which together with the high density demonstrated the feasibility of achieving transparent Al_2O_3 hemispheres by press forging.		

DD FORM 1473
1 JAN 64

Unclassified

Security Classification

Security Classification

14	KEY WORDS	LINK A		LINK B		LINK C	
		ROLE	WT	ROLE	WT	ROLE	WT

1. ORIGINATING ACTIVITY: Enter the name and address of the contractor, subcontractor, grantee, Department of Defense activity or other organization (corporate author) issuing the report.

2a. REPORT SECURITY CLASSIFICATION: Enter the overall security classification of the report. Indicate whether "Restricted Data" is included. Marking is to be in accordance with appropriate security regulations.

2b. GROUP: Automatic downgrading is specified in DoD Directive 5200.10 and Armed Forces Industrial Manual. Enter the group number. Also, when applicable, show that optional markings have been used for Group 3 and Group 4 as authorized.

3. **REPORT TITLE:** Enter the complete report title in all capital letters. Titles in all cases should be unclassified. If a meaningful title cannot be selected without classification, show title classification in all capitals in parenthesis immediately following the title.

4. **DESCRIPTIVE NOTES:** If appropriate, enter the type of report, e.g., interim, progress, summary, annual, or final. Give the inclusive dates when a specific reporting period is covered.

5. **AUTHOR(S):** Enter the name(s) of author(s) as shown on or in the report. Enter last name, first name, middle initial. If military, show rank and branch of service. The name of the principal author is an absolute minimum requirement.

6. **REPORT DATE:** Enter the date of the report as day, month, year; or month, year. If more than one date appears on the report, use date of publication.

7a. TOTAL NUMBER OF PAGES: The total page count should follow normal pagination procedures, i.e., enter the number of pages containing information.

7b. NUMBER OF REFERENCES: Enter the total number of references cited in the report.

8a. **CONTRACT OR GRANT NUMBER:** If appropriate, enter the applicable number of the contract or grant under which the report was written.

5b, 5c, & 5d. PROJECT NUMBER: Enter the appropriate military department identification, such as project number, subproject number, system numbers, task number, etc.

9a. ORIGINATOR'S REPORT NUMBER(S): Enter the official report number by which the document will be identified and controlled by the originating activity. This number must be unique to this report.

9b. OTHER REPORT NUMBER(S): If the report has been assigned any other report numbers (either by the originator or by the sponsor), also enter this number(s).

10. AVAILABILITY/LIMITATION NOTICES: Enter any limitations on further dissemination of the report, other than those indicated by the classification marking.

imposed by security classification, using standard statements such as:

- (1) "Qualified requesters may obtain copies of this report from DDC."
- (2) "Foreign announcement and dissemination of this report by DDC is not authorized."
- (3) "U. S. Government agencies may obtain copies of this report directly from DDC. Other qualified DDC users shall request through _____."
- (4) "U. S. military agencies may obtain copies of this report directly from DDC. Other qualified users shall request through _____."
- (5) "All circulation of this report is controlled. Qualified DDC users shall request through _____."

If the report has been furnished to the Office of Technical Services, Department of Commerce, for sale to the public, indicate this fact and enter the price, if known.

11. SUPPLEMENTARY NOTES: Use for additional explanatory notes.

12. SPONSORING MILITARY ACTIVITY: Enter the name of the departmental project office or laboratory sponsoring (paying for) the research and development. Include address.

13. ABSTRACT: Enter an abstract giving a brief and factual summary of the document indicative of the report, even though it may also appear elsewhere in the body of the technical report. If additional space is required, a continuation sheet shall be attached.

It is highly desirable that the abstract of classified reports be unclassified. Each paragraph of the abstract shall end with an indication of the military security classification of the information in the paragraph, represented as (TS), (S), (C), or (U).

There is no limitation on the length of the abstract. However, the suggested length is from 150 to 225 words.

14. KEY WORDS: Key words are technically meaningful terms or short phrases that characterize a report and may be used as index entries for cataloging the report. Key words must be selected with care. If a key word is required, Identifiers, such as equipment model designation, inventory, military project code name, geographic location, may be used as key words but will be followed by an indication of technical context. The assignment of links, rules, and weights is optional.

Security Classification

MICROSTRUCTURE STUDIES OF REFRACTORY

POLYCRYSTALLINE OXIDES

SUMMARY REPORT

1 April 1970 to 1 February 1971

Contract N00019-70-C-0171

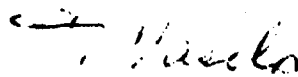
AVSD-0192-71-CR

Prepared for

U.S. Naval Air Systems
Washington 25, D.C.

APPROVED FOR PUBLIC RELEASE;
DISTRIBUTION UNLIMITED

Approved by



T. Vasilos

Prepared by

W.H. Rhodes
R.M. Cannon

AVCO CORPORATION
Systems Division
Lowell, Massachusetts 01851

FOREWORD

This report was prepared by the Systems Division of Avco Corporation under U.S. Navy Contract N00019-70-C-0171 entitled, Microstructure Studies of Polycrystalline Oxides.

The work was administered under the direction of the U.S. Department of the Navy, Air Systems Command, with Mr. Charles F. Bersch, Code AIR-52032A, acting as Project Engineer.

This report covers work conducted from 1 April 1970 to 1 February 1971.

The writers are pleased to acknowledge the contributions of the following individuals to this program; R. Gardner and P. Fuce for ceramic preparation, J. Centorino and E. Vallante for materials preparation. C.L. Houck for electron microscopy, P. Berneburg for x-ray studies and R.M. Haag, T. Vasilos and J. Niesse for useful discussions.

ABSTRACT

This study was concerned with the interaction between microstructure and chemistry in polycrystalline MgO and Al₂O₃ and several facets of mechanical properties. Further, the press forging of Al₂O₃ hemispheres was undertaken as earlier work had shown that press forging developed unique optical and mechanical properties.

A direct comparison of deformation in the high purity Al₂O₃ and less pure Al₂O₃ + 1/4% MgO with a nearly identical grain size and porosity demonstrated that the deformation rates were very close within a limited temperature regime. Several pieces of evidence to include a higher strain rate sensitivity which decreased with increasing temperature led to the conclusion that deformation in high purity fine-grained Al₂O₃ shifts from grain boundary diffusion to a strong component of grain boundary sliding at higher temperatures. The differences between the grades of Al₂O₃ were attributed to the influence of impurities and dopants on grain-to-grain bond strength.

Stress corrosion studies on two grades of hot pressed MgO and one grade of sintered MgO demonstrated marked differences among the grades and further differences in test environments known to react chemically and/or to influence dislocation mobilities in MgO. The corrosion curves as well as fractographic studies support the view that stress corrosion in H₂O is dominated by stress enhanced chemical corrosion which is strongly dependent on grain boundary impurity phases. Further, in the absence of H₂O a mechanical stress corrosion model may dominate as the static fatigue limit was influenced by organic media known to affect dislocation mobility.

The hemisphere press forging study was preliminary and mainly concerned with preform preparation, die design, lubrication and establishing process limits. The central zone of several hemispheres were crack-free and translucent with limited edge tearing. Also, a basal crystallographic texture parallel to the surface was developed which together with the high density demonstrated the feasibility of achieving transparent Al₂O₃ hemispheres by press forging.

TABLE OF CONTENTS

ABSTRACT

I. INTRODUCTION.	1
II. DEFORMATION OF HIGH PURITY MATERIAL	1
A. General	1
B. Material and Procedure.	2
1. Raw Material.	2
2. Test Procedure.	3
3. Analysis.	5
C. Results	5
D. Discussion.	11
E. Summary	16
III. STRESS CORROSION OF MAGNESIUM OXIDE	17
A. General	17
B. Material and Procedure.	18
1. Specimen Preparation.	18
2. Sample and Test and Environment Arrangement	19
3. Results	19
4. Discussion.	29
C. Summary and Conclusions	33
IV. PRESS FORGING ALUMINA HEMISPHERES	34
A. General	34
B. Material and Procedure.	35
1. Raw Material.	35
2. Forging Apparatus	37
3. Procedure	37
4. Analysis.	37

TABLE OF CONTENTS (Concl'd)

C. Results and Discussion.	39
D. Summary	55
V. REFERENCES.	56

LIST OF ILLUSTRATIONS

Figure No.

1	Microstructures of (a) High Purity Al_2O_3 on Ground Surface and (b) $\text{Al}_2\text{O}_3 + 1/4$ MgO on Fractured Surface. . . .	4
2	Stress-Strain Rate Curves for High Purity Al_2O_3	7
3	Tensile Surface (a) and Fractured Surface (b) of Deformed and Fractured High Purity Al_2O_3 Tested at 1270°C	8
4	Stress-Strain Rate Curves for Fine-Grained, Hot Pressed Material, Cl26C	9
5	Strain Rate Versus $1/T$ Showing the Activation Energy for Deformation at Two Stress Levels for High Purity $\text{Al}_2\text{O}_3 + 1/4$ w/o MgO	10
6	Dependence of the Activation Energy for Deformation on Grain Size.	12
7	Bend Strength as a Function of Temperature for Several Grades of Alumina	13
8	Product of Boundary Width Times Diffusion Coefficients versus Reciprocal Temperature for Deformation in Various Aluminas and Other Measurements	15
9	Typical Microstructure of Sintered MgO Showing Overall Single Phase Material, some Porosity and Second Phase Patches	20
10	Fractograph Showing Apparent Grain Boundary Phase in Sintered MgO.	20
11	Flaw Located at Fracture Interface of Sintered MgO.	23
12	Delayed Failure Curve for Honeywell Sintered MgO Tested in Distilled H_2O	24
13	Delayed Failure Curve for Honeywell Sintered MgO Tested in DMF.	25
14	Delayed Failure Curve for Honeywell Sintered MgO Tested in DMSO-10 v/o DMF.	26
15	Fractograph of Static Fatigue Specimen Tested in H_2O Exhibiting (A) Corroded Surface, (B) Secondary Cracks, and (C) River Marks	27
16	Fractograph of Static Fatigue Specimen Tested in H_2O Exhibiting (a) Pits Associated with Crack Arrest Lines and (b) Random Flat Bottom Pits on Grain Face	28

LIST OF ILLUSTRATIONS (Concl'd)

Figure No.

17	Fractograph of Static Fatigue Specimen Tested in DMF Showing Secondary Crack Associated with Pores.	30
18	Fractograph of Dynamically Argon Tested MgO Showing, (A) Secondary Cracks, (B) Textured Grain Face, (C) Cleavage Steps and (D) River Pattern	31
19	Delayed Failure Curves for Two Hot Pressed and One Sintered Grade MgO in Four Test Environments	32
20	Sectional View of Die, Al ₂ O ₃ Preform and Male and Female Punch	36
21	Record of Deflection and Pressure Versus Time in a Typical Hemisphere Forging Run	38
22	Initial Al ₂ O ₃ Hemisphere Forged from Powder.	41
23	Cross-Section of Hemispherical Forging D1432 Showing Second Phase Intrusions into Cracks.	41
24	Defects Noted in Early Al ₂ O ₃ Preforms; (a) Surface Cracks and (b) Internal Agglomerate Shrinkage, Cracks. . .	44
25	Cross-Section of Hemispherical Forging 1486 Showing Large-Grained Transparent Area and Textured Slightly Porous Area	47
26	Section of Press Forged Alumina Hemisphere 1493.	48
27	Second Phase Found Near Surface in One Local Area of Hemisphere 1493.	48
28	Entrapped Porosity Near One Edge Surface of Hemisphere 1493	49
29	Microstructure of Entire Cross-Section of Hemisphere 1493	50
30	Microstructure of Hemisphere 1497 Interrupted in Forging Showing, (a) Porosity Gradient and (b) Grain Size Gradient.	51
31	Thickness Profiles for Press Forged Al ₂ O ₃ Hemispheres. . .	53
32	Ratio of Relative X-ray Intensity for Center and Rim of Hemisphere 1432	54

LIST OF TABLES

Table No.

I	Deformation Models and Their Grain Size and Strain Rate Dependence.	2
II	Dynamic Room Temperature Strength of Sintered MgO	21
III	Delayed Fracture Tests on Sintered MgO.	22
IV	Hemispherical Forging Experiments	40
V	Preform Preparation and Results after Short Sinter.	42

I. INTRODUCTION

It is generally agreed that there is an intimate dependence of mechanical properties on chemistry, microstructure and process technique for ceramic products. This program was concerned with two aspects of this very broad problem; 1) the plastic deformation of fine-grained high purity hot pressed Al_2O_3 as compared with similarly processed but lower purity material and 2) the stress corrosion of polycrystalline MgO and whether a chemical or mechanical (dislocation) model for failure applies. These studies have been carried on for several years and are now at a point where conclusions can be drawn. This report will summarize the earlier work as well as present the new studies.

The final area of investigation was a process related study resulting from earlier work demonstrating the unique optical and mechanical properties of press-forged Al_2O_3 . The goal of the process study was the achievement of a transparent, fine to medium grain sized Al_2O_3 hemisphere by press forging.

II. DEFORMATION OF HIGH PURITY MATERIAL

A. General

The lack of sufficiently pure polycrystalline Al_2O_3 has made it impossible to distinguish between structure-sensitive and composition-sensitive mechanical behavior. Composition can be expected to affect the point defect concentration, width of a segregated zone near grain boundaries, and finally, presence of grain boundary phases. Each of the possible polycrystalline deformation mechanisms could be composition or purity dependent. Slip by dislocation flow is known to be influenced by impurities as the Peierl stress for the initiation of dislocation motion is affected by the spacing and size of the impurity ions as well as associated point defects. Grain boundary sliding could be influenced by impurities in several ways. If the impurities actually formed a second phase this could impede grain boundary sliding in the case of a non-wetting phase with higher flow stresses than the matrix or on the other hand, enhance grain boundary sliding in the case of a low flow stress wetting second phase. Also, grain boundary sliding may be controlled by diffusion of a species around a ledge and this rate would be influenced by the defect layer adjacent to the boundary. Grain boundary sliding by a dislocation model must involve impurity dependent processes as most dislocation processes are impurity dependent. Finally, it must be assumed that either lattice or boundary diffusion mechanisms of deformation will be dependent on impurity concentration as it is assumed that with the possible exception of some $0-2$ measurements(1) diffusion coefficients measured to date represent extrinsic (impurity dependent) diffusion. Models for the three main deformation mechanisms possess different predicted strain rate and grain size dependencies as noted in Table I. Thus, testing high purity Al_2O_3 and comparing the strain rate dependencies with less pure Al_2O_3 having as near as possible an identical microstructure has the potential of shedding new insight into the dominant mode of deformation. The study did not include a comparison of grain size dependencies, but enough information was obtained to know that it was the same sign as less pure Al_2O_3 .

The deformation of $\text{Al}_2\text{O}_3 + 1/4$ w/o MgO has been under study at this

TABLE I
DEFORMATION MODELS AND THEIR GRAIN SIZE AND
STRAIN RATE DEPENDENCE

Deformation Model	Reference	Exponential Coefficient*	
		Strain Rate Parameter	Grain Size Parameter
Dislocation model	4,5	0.2 to 0.4	0 to -2
Deformation twinning	2		
Kinking	2,6		
Diffusional creep			
a. Lattice path	7	1	2
b. Boundary path	8	1	3
Boundary sliding	9,10	0.2 to 1	1 to 2

* The parameters "m" and "a" in $\sigma = K\epsilon^m$ and $\epsilon \sim G.S.^{-a}$

laboratory for several years.(2,3) It was found that the strain rate exponent, m, rose from ~ 0.61 to 0.95 with increasing grain size from 1.2 to 15 micron grain size. In turn a grain size exponent of a ≈ 2.5 was found. Examination of the models in Table I would indicate that deformation in fine-grained alumina occurs by grain boundary sliding. The change in macroscopic flow parameters would indicate that with increasing grain size flow becomes increasingly controlled by diffusion. At the 1-2 micron grain size, microscopic evidence such as offset and distorted triple junctions, and wavy, distorted or indistinct grain boundaries provide strong indication that the deformation is dominated by grain boundary sliding. Further, there was a strong indication that slip plays a significant part in the accommodation process. In the coarser-grained alumina where m values near unity were found, the deformation appears to be controlled by diffusional creep. The fact that the activation energy ΔH continues to increase in excess of 2 in the range of 7-34 micron may be evidence of a contribution of grain boundary diffusion to the diffusional creep or it may be as a result of grain boundary sliding in a way not clearly understood. Diffusional creep requires grain boundary sliding for accommodation and it is not obvious whether this occurs by a diffusional mechanism or by one of the boundary sliding models. With this summary of deformation in $Al_2O_3 + 1/4\%$ as a basis for comparison the results on high purity Al_2O_3 are presented.

B. Material and Procedure

1. Raw Material

All high purity Al_2O_3 samples were fabricated from one powder lot.*

* Lot S5578 supplied by United Mineral, Distributor for Johnson-Matthey with a reported purity of 99.9995% Al_2O_3 .

Particulate properties, powder chemistry and fabrication procedure were previously studied.^(11,12,13) Quantitative x-ray analysis established the powder to be 58 w/o α Al_2O_3 with the remainder transitional, mainly γ Al_2O_3 . A bimodal particle size distribution was found with mean particulate diameters of 1500 \AA and 240 \AA for the two phases, respectively. Spark source mass spectrographic analysis (in contrast to the suppliers emission spectrographic analysis) reported total impurities (cations and anions) of 914 ppm, 305 ppm and 121 ppm for the powder, hot pressed billet and annealed specimens, respectively. The cation impurities alone were about 80 ppm. The hot pressing conditions were 1400°C, 15 Kpsi, 10 minutes giving a relative density of 99.7% of theoretical and a grain intercept of 0.75 - 0.83 microns (grain size of 1.12-1.24 microns).

Efforts to supplement the original supply of high purity Al_2O_3 were notably unsuccessful. The supplemental batches received have had too large a particle size thus negating efforts to achieve high density and fine grain size together. This is a fair indication of the difficulty in running a high purity program and achieving meaningful and comparable test results. All of the high purity Al_2O_3 results were conducted on specimens fabricated from the original powder lot.

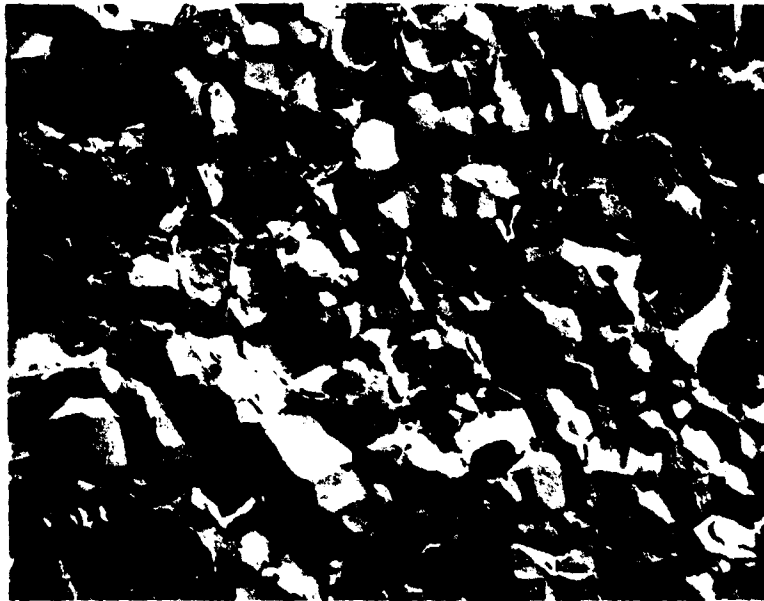
For comparison, tests were also conducted on 99.97% Al_2O_3 + 1/4 w/o MgO specimens (Billet C126). This billet was 99.7% dense with a grain intercept of 0.8 microns (grain size of 1.2 microns) which was very close to the grain size of the high purity Al_2O_3 . This material had been extensively tested on another program,⁽³⁾ but in a different apparatus and different specimen size than that used for the high purity Al_2O_3 tests. Thus, continued testing aided in the development of self-consistent test results for the two pieces of apparatus. It was also fortunate that the grain sizes and densities were close to being identical as this greatly aided in a comparison of deformation properties. The two microstructures are shown in Figure 1.

2. Test Procedure

Samples with different cross-sections (0.050 x 0.125 or 0.030 x 0.070 inches) and 0.875 inches long were tested in 4-point bending. A molybdenum resistance furnace and argon test environment was employed. (A zirconia insulation* replaced alumina silicate which had been used outside the heat shields in the earlier work.) The bend fixture was constructed from TZM and small radius sapphire knife edges were used (extensive testing with a variety of candidate materials demonstrated these to have superior sliding frictional properties). A tungsten strain measuring probe (referenced to the lower knife edge block) was coupled with a LVDT and recorder for strain and strain rate measurements. Considerable care was taken to eliminate spurious loads or bellows friction problems. Both load and deformation were recorded separately versus time. Machined specimens were cleaned in HF-HNO₃, H₂O and ethanol and handled only with teflon tweezers or while wearing white gloves.

The normal practice was to strain the specimen to the limit of the bend fixture (5% for the 0.050 x 0.125 cross-section and 2.5% for the 0.030 x 0.070 cross-section) at a constant strain rate. Several tests were

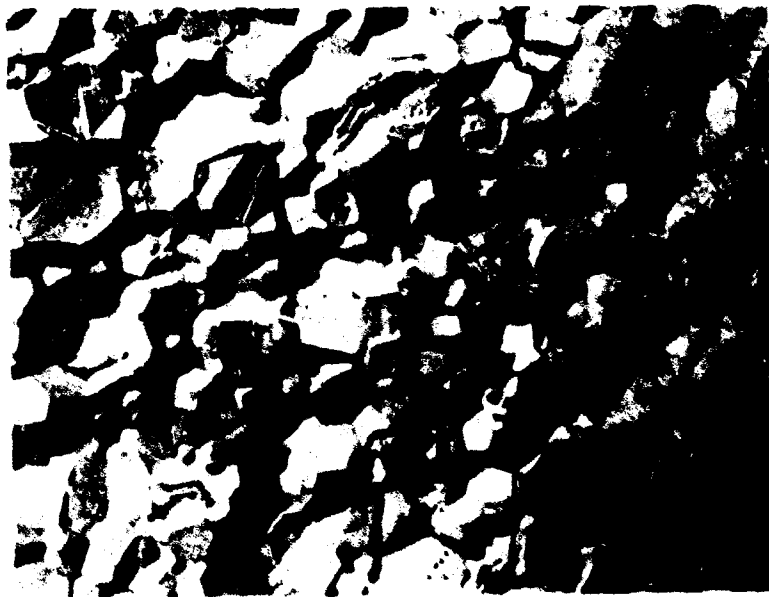
* Zircor, Union Carbide Corp.



#691233

(a)

7500X



#70578A

(b)

7500X

Figure 1. Microstructures of (a) High Purity Al_2O_3 on Ground Surface and (b) $\text{Al}_2\text{O}_3 + 1/4 \text{ MgO}$ on Fractured Surface.

conducted by changing strain rate once steady-state stress (within the 2% limit) was reached. An analysis of the effect of knife edge friction⁽³⁾ demonstrated that the true moment is a strong function of both the friction coefficient and percent strain. Since the friction during test was unknown, flow stress measurements were taken within the first 2% strain.

Microstructural changes were sought after each test by a fractographic examination of either or both the tension and compression surface and the fracture surface. Unbroken specimens were sectioned and checked for grain size changes.

3. Analysis

The analysis of the load-deflection data for plastic bending requires consideration beyond the elastic analysis. This results because the flow stress is, in general, a function of both strain and strain rate, and is not necessarily linear through the beam, thus invalidating the elastic stress analysis. When the stress is independent of strain and is linearly proportional to the strain rate, as in diffusional creep, the stress distribution is linear in the beam and the elastic equation may be used.⁽¹⁴⁾

A procedure has been developed for determining the stress-strain-strain rate relations for materials which strain harden and are rate sensitive.⁽¹⁵⁾ This requires the measurement of the bending moment as a function of deflection and deflection rate and the determination of the outer fiber stress from the relation:

$$\sigma = \frac{M}{bh^2} (2 + n_b + m_b) \quad (1)$$

$$\text{where } n_b = \left(\frac{\int \ln M}{\int \ln \phi} \right) \phi \quad (2)$$

$$m_b = \left(\frac{\int \ln M}{\int \ln \dot{\phi}} \right) \dot{\phi} \quad (3)$$

where M is the bending moment, ϕ the angle of inclination of the neutral axis of the beam (proportional to the deflection), $\dot{\phi}$ the rate of change of ϕ , and b and h are the width and depth of the beam. The strain and strain rate are determined directly from the deflection by geometrical considerations. During a test the load and the deflection are continuously recorded versus time and the "outer fiber" stress-strain curve, and strain rate are calculated from this data. In general, a series of constant rate bend tests are made from which the desired relations are calculated.

C. Results

The moment versus ϕ curves were checked for any strain hardening and it was determined that within 2% strain $n_b = 0$. Next, M versus curves were plotted and the values of m_b were calculated for each temperature. Using Equation (1) steady-state stress was calculated and this was plotted

versus strain rate, Figure 2. 1350°C was the highest temperature at which data could be collected without grain growth. In the previous year's results, data was presented for 1400°C and measurements were attempted at 1450 and 1480°C. Growth had increased the grain intercept to 1.5 and 3 microns during the 1400 and 1450°C tests, respectively; thus, data at these temperatures and above were not fully analyzed.* Grain growth increased the flow stress thus confirming the sign to the grain size dependence as obtained for the less pure Al₂O₃. Some of the scatter in the 1350°C data may be a result of slight grain growth although fractographic examination revealed a post-test grain intercept of $0.8 \pm 0.1 \mu\text{m}$, a value thought to be within the scatter of the grain sizes for the starting material. No grain growth was detected on samples tested at lower temperatures.

A typical tensile surface structure is shown in Figure 3a. All the surfaces are free of the singularities discussed in the previous report.⁽¹¹⁾ This may be a result of using a cleaner insulation material in the test furnace. Figure 3b illustrates a typical fracture surface. There is some evidence (at arrow) for a double boundary effect. This was discussed previously⁽¹¹⁾ with a higher magnification view, but briefly suggests extensive shear as typified by dislocation interactions with grain boundaries or grain boundary migration and etching of a ghost boundary.

Data collected during this and a related⁽³⁾ program on 1.2 μm grain size Al₂O₃ + 1/4 w/o MgO are presented in Figure 4. This data was analyzed using an identical method to that described above. The data at 1291°C and 1397°C was taken on small specimens in the same apparatus as the high purity Al₂O₃ specimens. The remaining data was taken for large specimens; however, both pieces of apparatus used the same argon atmosphere.

A direct assessment of the intra-machine reliability and calibration was achieved by plotting the strain rate at two flow stresses versus reciprocal temperature, Figure 5. Also, on this graph appears the data for high purity Al₂O₃. But, first consider just the Al₂O₃ + 1/4 MgO data. A very good straight line fit was achieved for the four highest temperature points at both flow stresses. This demonstrated that temperature, stress and strain calibrations were consistent for both units and further, that as far as the machine parameters are concerned, the data on the Al₂O₃ + 1/4 w/o MgO could be used for comparison with the high purity Al₂O₃.

The most striking feature of Figure 5 is the nearly identical flow properties of the two materials. Considering first the 20 Kpsi flow stress curve, the activation energies are 115 Kcal and 91 Kcal for the low and high purity material, respectively. The separation of the curves must be viewed with some uncertainty due to the lack of low temperature data for Al₂O₃ + 1/4 w/o MgO samples. Actual data was obtained at 20 Kpsi stress for both materials at all but the highest temperature (where extrapolation was required). The strain rate points at 10 Kpsi represent actual data points for the Al₂O₃ + 1/4 MgO, but required an extrapolation on the

* A flow stress at 1400°C corrected for grain growth was calculated previously, but it was withdrawn from the detailed analysis because of the uncertainty of grain growth.

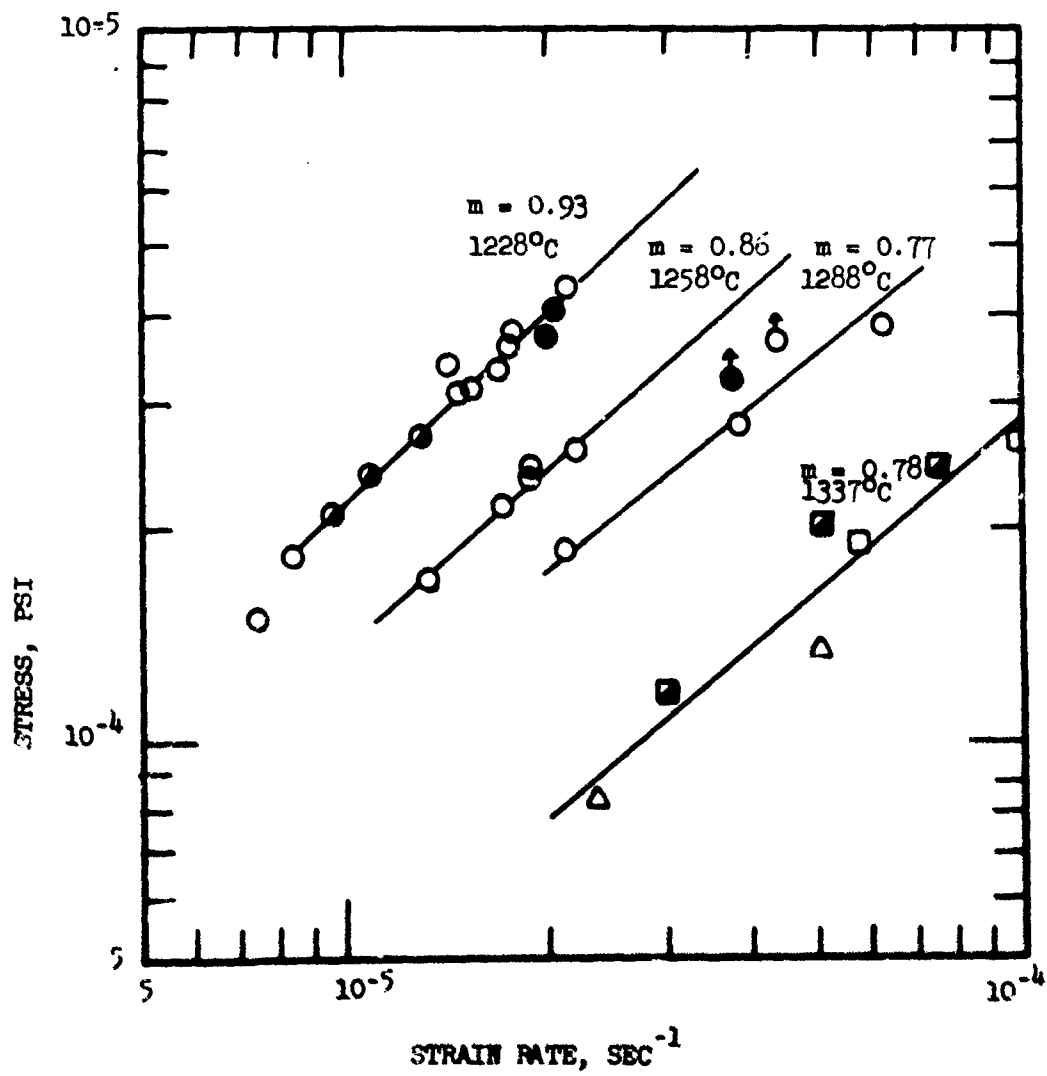
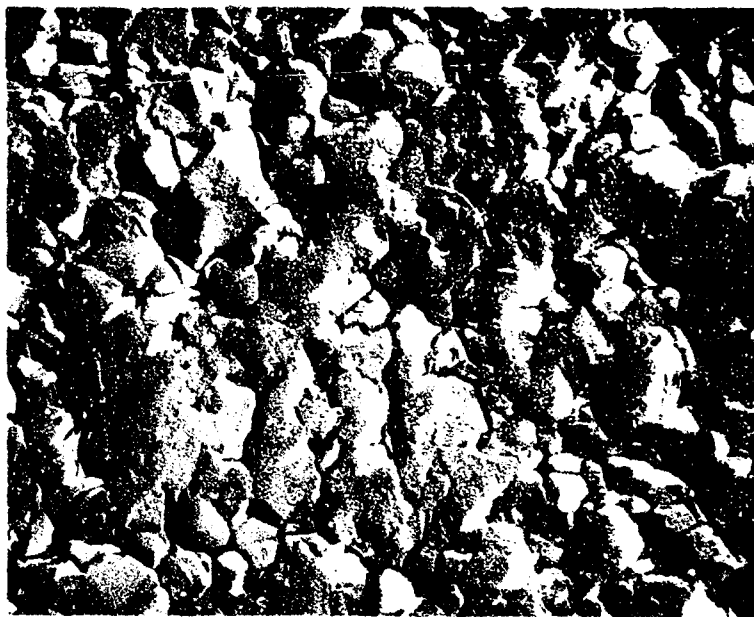


Figure 2. Stress-Strain Rate Curves for High Purity Al₂O₃.



#71034

(a)

7500X



#71031

(b)

15,000X

Figure 3. Tensile Surface (a) and Fractured Surface (b) of Deformed and Fractured High Purity Al_2O_3 Tested at 1270°C .

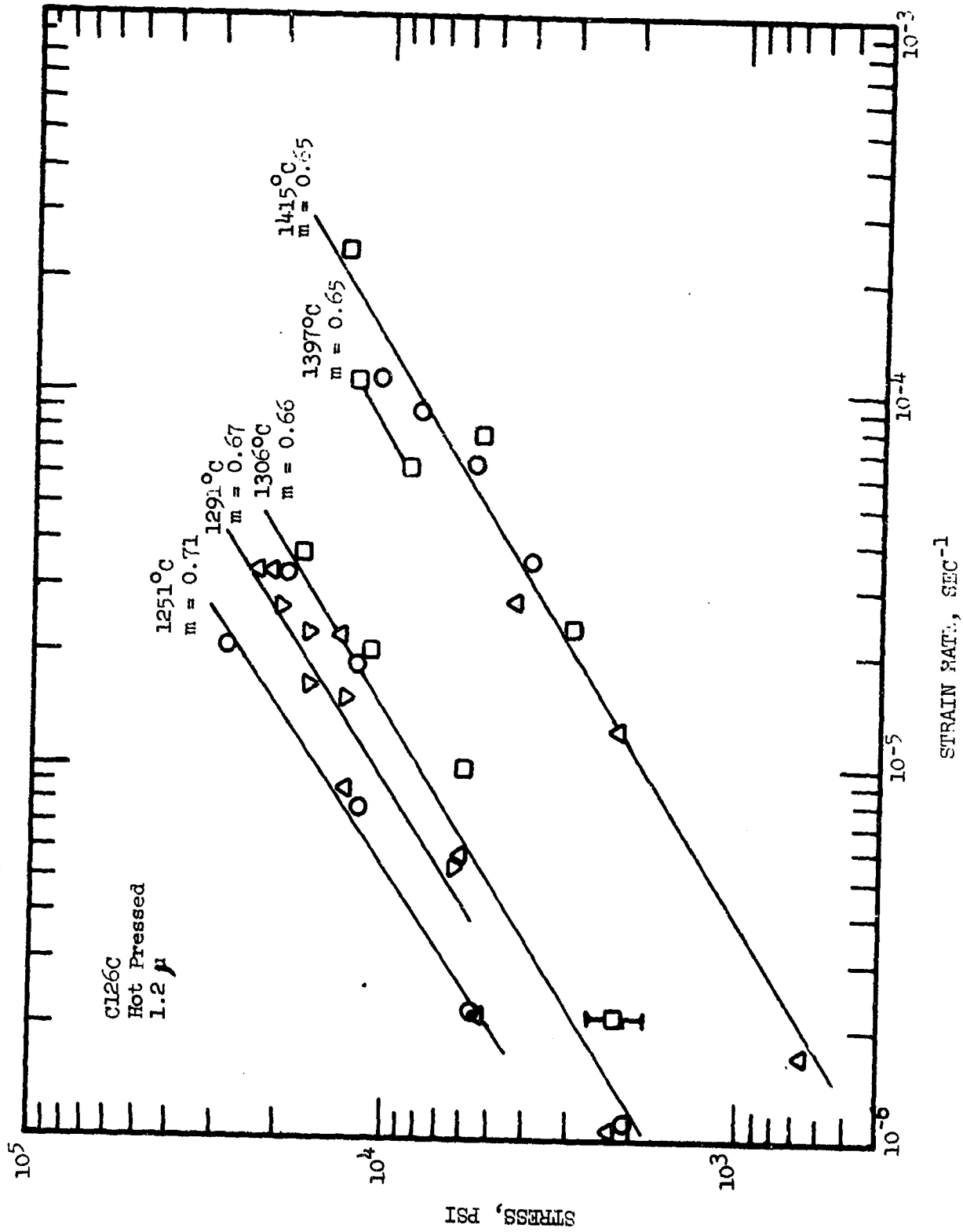


Figure 4. Stress-Strain Rate Curves for Fine-Grained, Hot Pressed Material. Cl26C.

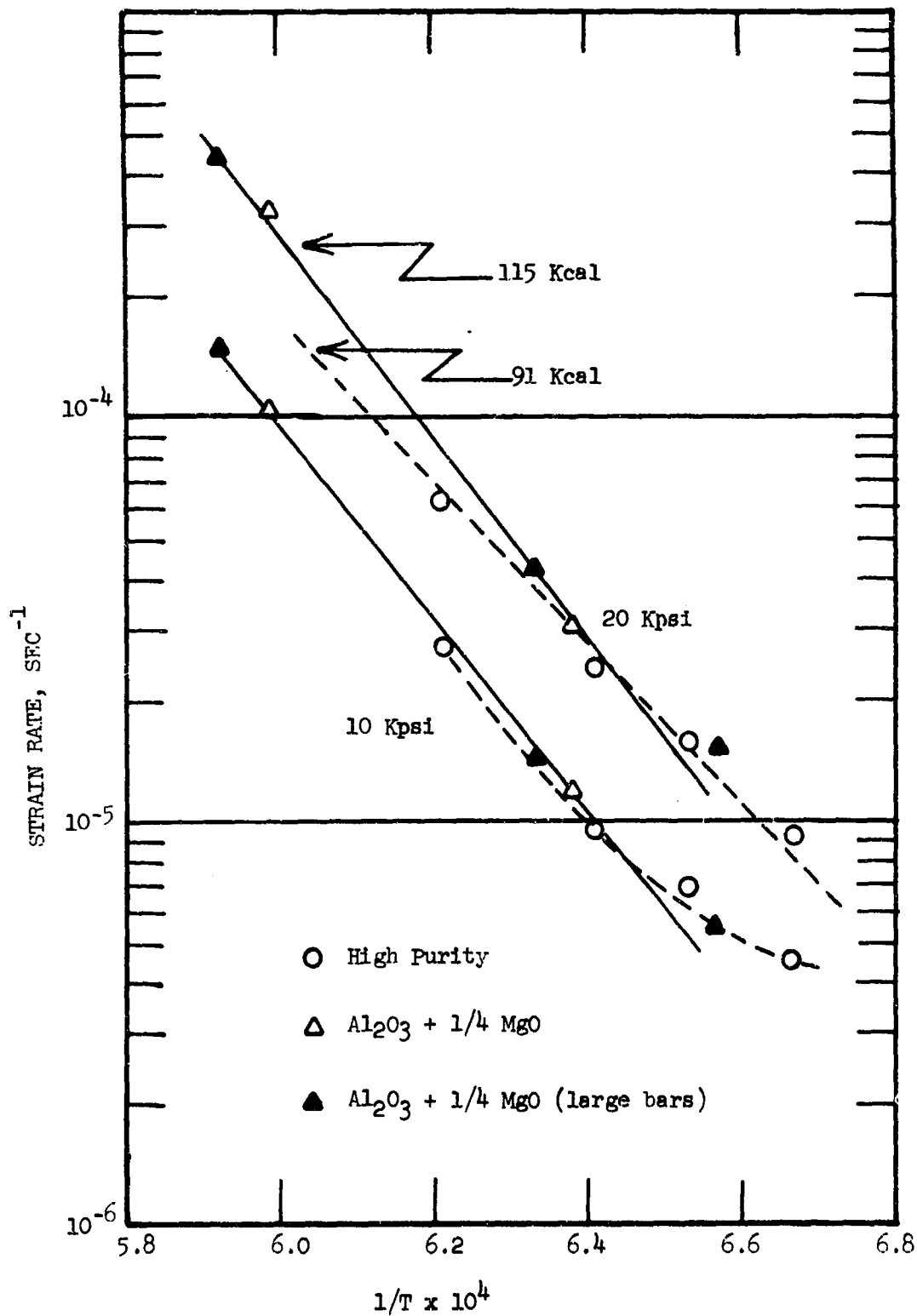


Figure 5. Strain Rate Versus 1/T Showing the Activation Energy for Deformation at Two Stress Levels for High Purity Al₂O₃ + 1/4 w/o MgO.

high purity Al_2O_3 . The increasing slope of the $\log \sigma \log \dot{\epsilon}$ curve with decreasing temperature had the effect of exhibiting curvature in the ΔH curve. It is also thought to be noteworthy that the lowest temperature strain rate point (at both 20 Kpsi and 10 Kpsi) for the $\text{Al}_2\text{O}_3 + 1/4 \text{ MgO}$ material was above the best line for the remainder of the temperature.

It was shown previously, (2,3) that activation energy for creep increased with increasing grain size. This finding is substantiated by the present results, Figure 6, with the additional feature that the high purity Al_2O_3 possesses a lower activation energy than the $\text{Al}_2\text{O}_3 + 1/4 \text{ MgO}$ body.

The fracture strength determinations resulting from the conclusion of the deformation tests together with the data previously presented⁽¹¹⁾ are compared with results of Spriggs, Mitchell and Vasilos⁽¹⁶⁾ on 99.9% Al_2O_3 , Figure 7. Also included are recent data on Al_2O_3 and $1/4\%$ MgO. All of these data were calculated using the elastic fracture formula. The data show the high purity material to be about the same or slightly less strong in the 1200-1400°C range and somewhat stronger at temperatures greater than 1400°C.

D. Discussion

The preliminary results on high purity Al_2O_3 ⁽¹¹⁾ suggested that the creep rate was significantly lower for this material than $\text{Al}_2\text{O}_3 + 1/4 \text{ w/o MgO}$. This was not substantiated by the recent work. In large part, the difference in creep rate was removed by careful temperature calibration of both testing systems and the availability of $\text{Al}_2\text{O}_3 + 1/4 \text{ MgO}$ with an identical microstructure to the high purity Al_2O_3 . However, several significant differences between the material exist and the discussion will center on the following differences and the general implications of these features on deformation in Al_2O_3 :

- . Higher strain rate sensitivity (higher m_b)
- . An increasing m_b with decreasing temperature

Several additional observations appear to be unique to the high purity Al_2O_3 ; however, in these cases the arguments must be tempered with the statement that the $\text{Al}_2\text{O}_3 + 1/4 \text{ w/o MgO}$ specimens may show similar trends with more extensive low temperature testing. These features are:

- . A temperature-dependent activation energy
- . A lower activation energy

Non-Newtonian grain boundary sliding is probably the principal cause of $m_b < 1$ in fine-grain Al_2O_3 . Arguments were recently presented that may also involve the movement of dislocations in the boundaries. It was previously shown that increasing grain size results in increasing m_b values (in the direction of Newtonian process). Now it appears that increasing purity has a similar effect.

The increase in m_b with increased purity is most likely due to a shift away from grain boundary sliding deformation control. It is reasonable

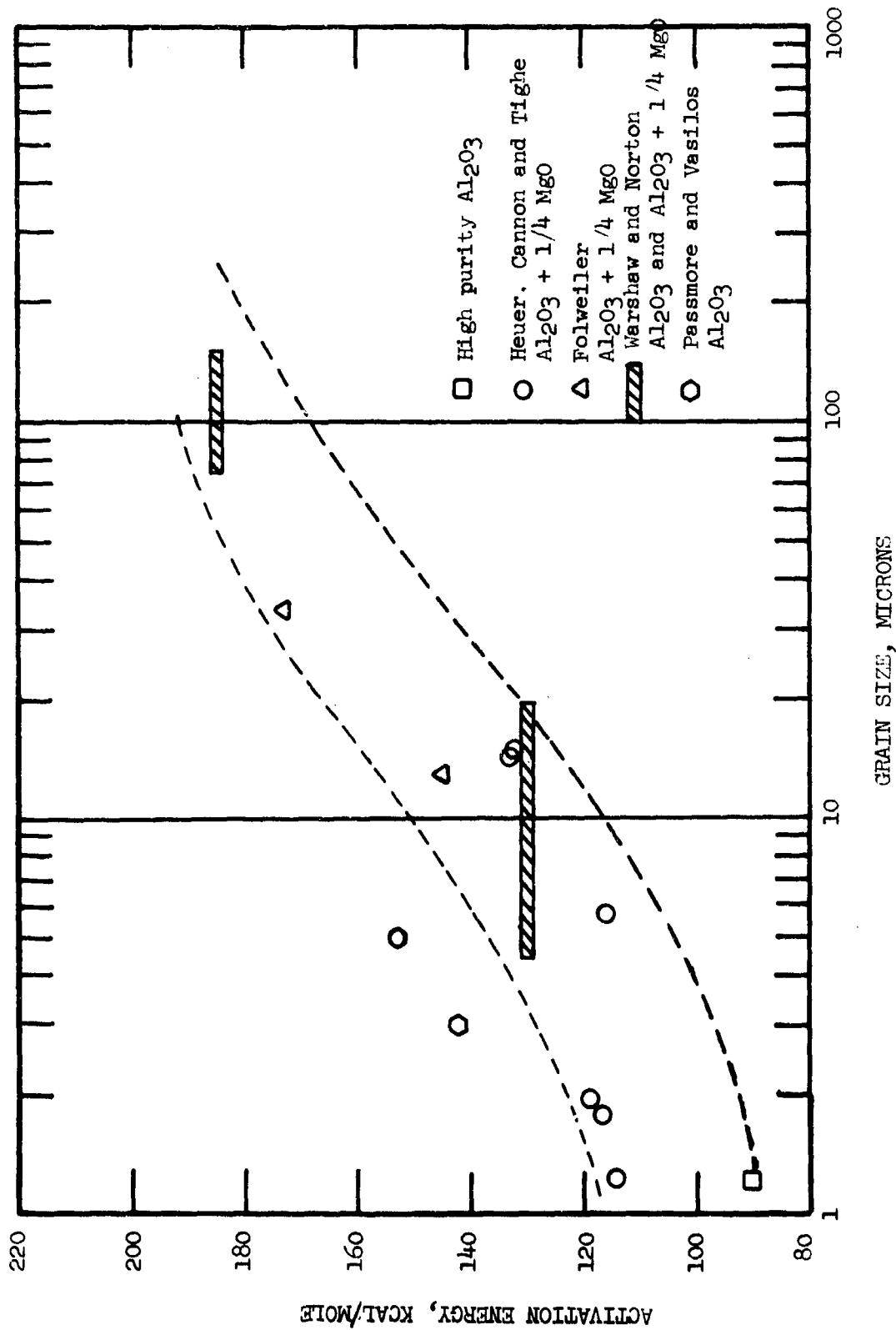


Figure 6. Dependence of the Activation Energy for Deformation on Grain Size. The grain sizes for the various investigators have been normalized to the same correction factor. The values from Folweiler's data were determined by the present authors.

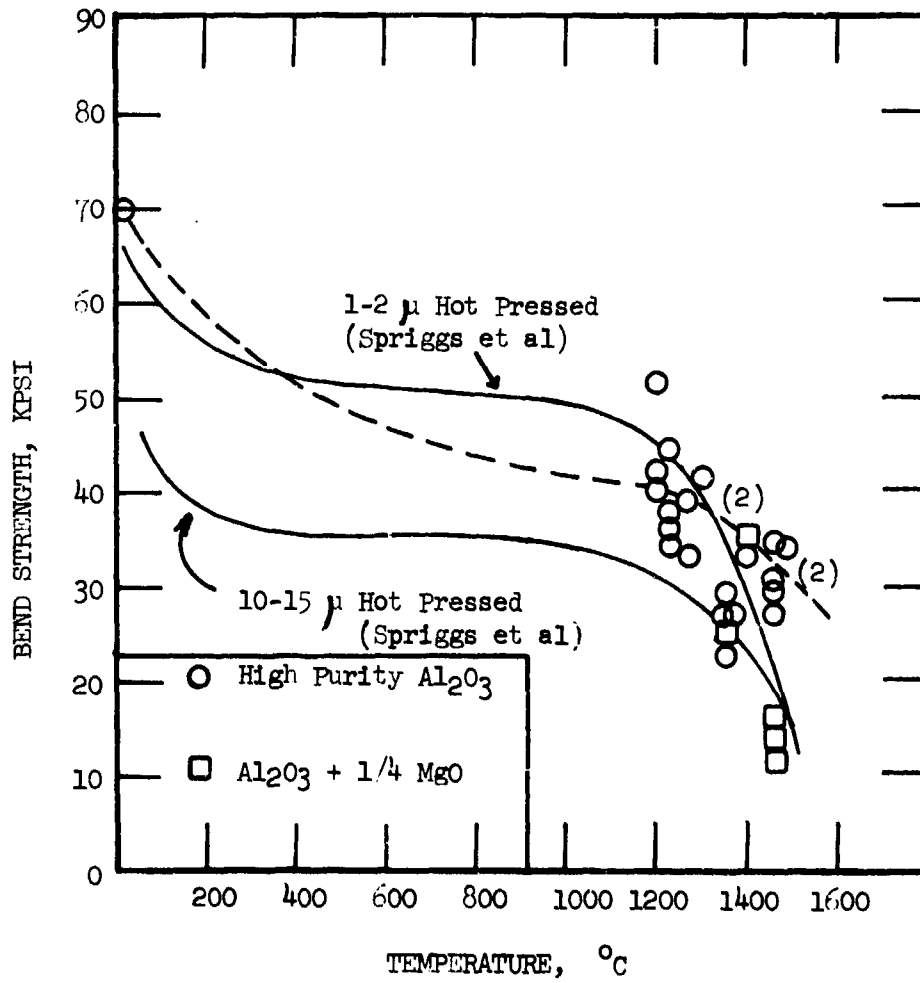


Figure 7. Bend Strength as a Function of Temperature for Several Grades of Alumina

to expect this to be the case if one assumes that impurities are segregated at grain boundaries. Jorgensen⁽¹⁷⁾ has argued convincingly for segregation of Mg^{+2} toward Al_2O_3 grain boundaries and thermodynamics would predict this to be the case for the other impurities as well. Arguments concerning the controlling deformation mechanism will be withheld until several other points are discussed.

As shown in Figure 2 the strain rate sensitivity, m_p , increase further with decreasing test temperature. This condition has not been encountered in deformation testing of other fine-grained Al_2O_3 ^(2,3) where the strain rate sensitivity and activation energy remained constant over the temperature range tested. This shift, of course, is also in the direction of a Newtonian process. In fact, at the lowest temperature tested, 1228°C, the strain rate sensitivity is very close to being Newtonian. This is the strain rate sensitivity expected for diffusional creep^(7,8) or that predicted by a grain boundary sliding model which involves diffusional mass transport for the necessary accommodation.⁽⁹⁾

It would appear that this shift to high m_p at low temperatures is due to a shift in rate controlling mechanism rather than from one type of grain boundary sliding to another. Support for this comes from the slight curvature in the activation energy plot, Figure 5. Thus, it is argued that the increasing m_p at low temperature is due to a shift in controlling mechanism away from non-Newtonian grain boundary sliding toward diffusional creep. An examination of previous results on creep and diffusion related processes in Al_2O_3 provides insight into whether grain boundary or lattice diffusion is the controlling process.

As shown in Figure 6, the activation energy for creep with $m_p > 0.5$ falls from about 175 Kcal/mole at very coarse grain sizes to about 115 Kcal/mole for 1.2 μm $Al_2O_3 + 1/4$ MgO. For these studies the m_p fell from about $m_p \approx 1$, a 30 μm to $m_p \approx 0.65$ at grain sizes less than 5 μm . The fall in activation energy was about what would be expected in a shift from lattice to grain boundary diffusion controlled, but since this was accompanied by a reduction in m_p it was argued⁽²⁾ that the concurrent shifts were due to a change in rate controlling mechanism (from diffusional creep to grain boundary sliding with a contribution due to slip and perhaps diffusion). Now in the case of high purity 1.2 μm material, where the activation energy is even lower at 91 Kcal/mole, the condition of high m_p has returned. Thus, it seems reasonable to project that this results from a shift to grain boundary diffusion controlled creep where a high m_p is predicted (Table I).

The Coble⁽⁸⁾ treatment of the Nabarro-Herring model based on boundary diffusion gives

$$\dot{\epsilon} = \frac{47.1 w D_b}{kT G^3} \quad (4)$$

where w is the boundary width and D_b the diffusion coefficient. The combined factor $w D_b$ is shown in Figure 8 with creep data analyzed in an identical manner and $w D_b$ factors from secondary grain growth studies by Mistler⁽²¹⁾ initial sintering kinetics by Johnson and Berrin⁽²²⁾ and creep

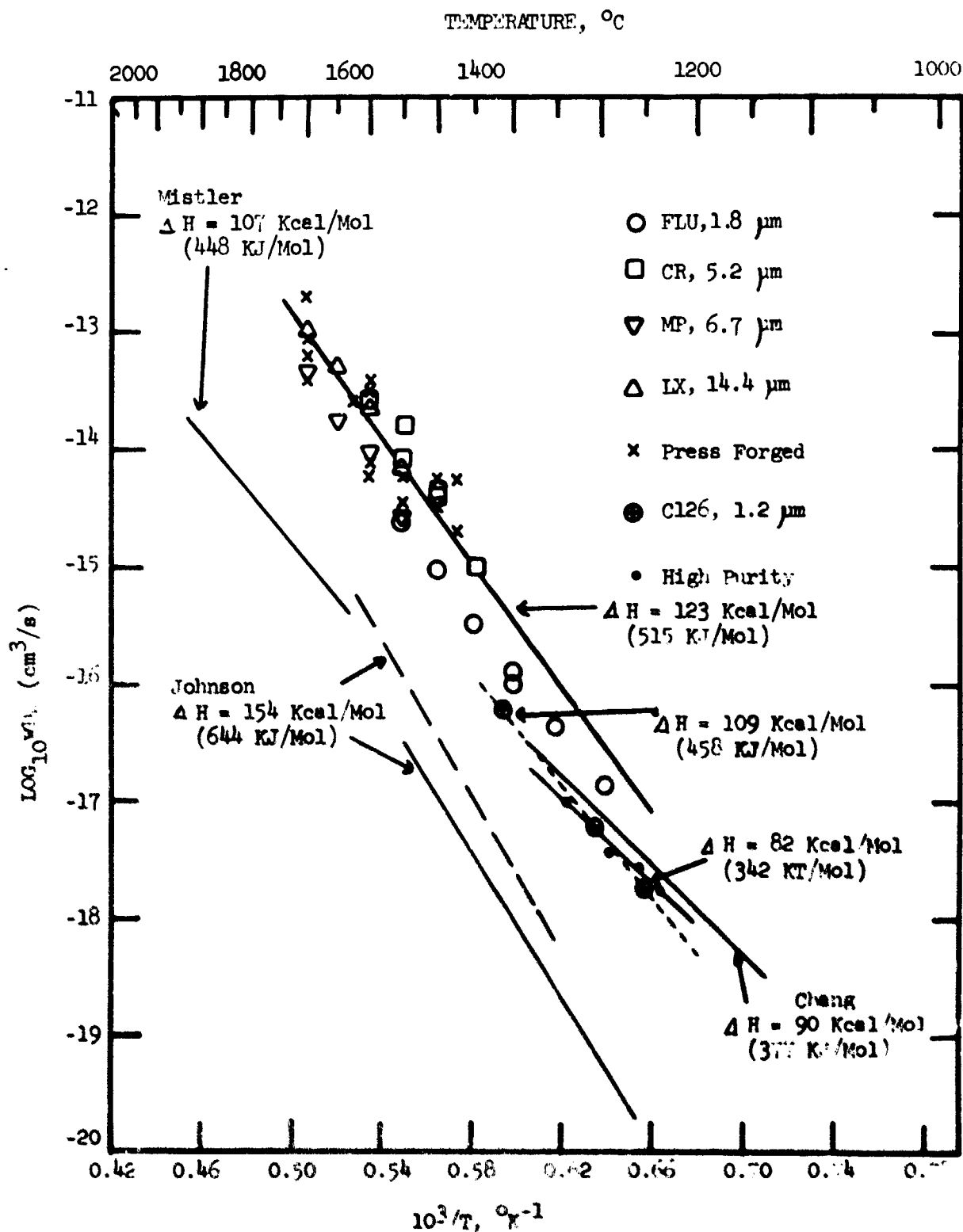


Figure 8. Product of Boundary Width Times Diffusion Coefficients versus Reciprocal Temperature for Deformation in Various Aluminas and Other Measurements.

data of Chang.⁽²³⁾ In general, the line for the high purity Al_2O_3 was quite distinct from the band of data for standard Al_2O_3 . The Cl26 data discussed in this report fell quite close to the high purity Al_2O_3 as would be expected from Figure 5. The fact that the line fell below the bulk of the standard Al_2O_3 data and corresponded both in level and activation energy with that of Chang lends further support for a shift with decreasing temperature to grain boundary controlled creep for high purity Al_2O_3 .

It is interesting to speculate on the reason for decreased grain boundary sliding with increased purity. With increasing impurities at the grain boundary the grain to grain bond strength generally decreases while the local defect concentration increases. If grain boundary sliding was controlled by a grain boundary dislocation model, the high defect concentration might be expected to impede dislocation motion; in this case, increasing purity would favor increased dislocation controlled grain boundary sliding. Since the opposite effect occurred, it would appear that the grain to grain bond strength is more influential in controlling sliding. At the highest temperatures tested grain boundary sliding still contributed to the deformation process, in high purity Al_2O_3 (as evidenced by the low m_b), but as test temperature was lowered a slower process became rate controlling presumably due to a rapidly increasing grain to grain bond strength.

The strength data in Figure 7 show the high purity material to be about the same or slightly less strong in the 1200-1400°C range and somewhat stronger at temperatures greater than 1400°C. The decreased strengths are in part a result of the fact that the high purity Al_2O_3 had a smaller grain size and consequently, a lower flow stress than the Al_2O_3 of Spriggs et al.⁽¹⁶⁾ Conversely, the higher strength values may partially be a result of the fact that grain growth hardened the high purity material at 1400°C and above. It is noteworthy, however, that strengths in this range were above those obtained for the 10-15 micron material of Spriggs et al. It appears that the decreased tendency for grain boundary sliding in high purity contributes along with the grain size effects noted above to the high strengths.

E. Summary

1. Deformation studies were conducted on uniform 1.2 μm grain size 99.8% dense Al_2O_3 having up to 300 ppm total and 80 ppm cation impurities as detected by spark source mass spectroscopy. Early work by plasma source mass spectroscopy had shown these impurities to be inhomogeneously distributed.
2. A direct comparison of deformation in the high purity material and less pure $\text{Al}_2\text{O}_3 + 1/4\%$ MgO revealed very similar deformation rates where measurements coincided. Several important differences were found, however; (a) the strain rate sensitivity was higher, (b) the strain rate sensitivity increased further with decreasing temperature, (c) the activation energy was temperature-dependent and (d) the apparent activation energy was lower. These results led to the conclusion that deformation in high purity fine-grained Al_2O_3 is controlled more by a

diffusional creep process than by grain boundary sliding. The increased purity effectively causing the mechanism to shift away from grain boundary sliding which is strong in the less pure material. Diffusional creep becomes more dominant at low temperatures, for high purity Al_2O_3 , and further it would appear from the low activation energy that the process is grain boundary diffusion rather than lattice diffusion controlled.

III. STRESS CORROSION OF MAGNESIUM OXIDE

A. General

Stress corrosion cracking is a well-known phenomena that is controlled by mechanical or chemical processes occurring at the interface between the solid and the environment. Under some conditions, the surface reaction can be beneficial, i.e., the Joffe's effect where dissolution increased the crack tip radius thereby blunting a potential critical crack. In most cases the surface reaction degrades the usable strength and, consequently, knowledge of such reactions is important for structural materials. There are two major classes of models governing the advancement of the stress corrosion crack; 1) those which postulate crack advancement by stress enhanced chemical dissolution at the tip - the point of highest chemical potential and 2) those which involve only mechanical phenomena such as mobile dislocations or reduction of the surface energy term in the Griffith relationship.

Moderate strain rate testing in earlier efforts^(12,13) on polycrystalline MgO had led to the following general conclusions; 1) stress corrosion did not occur in MgO at room temperature at testing strain rates in the order $5 \times 10^{-3}/\text{min.}$, 2) room temperature fractures were nucleated by mobile dislocations; hence, high strengths were obtained in both air and argon for annealed specimens. Thus, the room temperature strength was not particularly sensitive to the initial crack length although it was not possible to say whether it was strictly due to the Griffith criteria or if the dislocation mechanism of Clarke et al⁽²⁴⁾ was dominant. At liquid N_2 temperature the mechanically polished samples which certainly contained fresh dislocations showed significantly higher strengths than surfaces with greater crack lengths. This suggested that the classic Griffith relation holds at 77°K , rather than a dislocation crack nucleation process.

Recently^(11,12) dead-load stress corrosion tests were conducted on MgO similar to the type referenced above in a H_2O environment and MgO hot pressed by the LiF additive process in both a H_2O and 1M $(\text{CH}_3)_2\text{NCHO}$, dimethyl formamide (DMF) environment. A pronounced delayed failure curve was observed in all tests although the slopes were quite different for the three test conditions. DMF was chosen as a test environment as Westwood^(25,26) has demonstrated that complexes of a high positive or negative charge significantly enhance dislocation mobility (the Rebinder effect). Thus, the test environments were chosen to aid in establishing whether stress corrosion was due to a chemical or mechanical model in MgO. The fact that the two types of MgO gave quite different results in the H_2O environment suggested that the chemistries were significantly different and perhaps responsible for the varying stress corrosion behavior. Electron microscopic

examination revealed that very thin ($\sim 0.1 \mu\text{m}$) grain boundary phases were present in at least some of the boundaries in both types of hot pressed MgO. In the case of undoped MgO fabricated from Fisher MgO, electron diffraction identified $\text{Na}_6\text{Al}_4\text{Si}_4\text{O}_{17}$ as the boundary phase. The boundary phase was not identified in the LiF doped MgO. Other investigators (27,28) have detected concentrations of Ca and Si at MgO grain boundaries by microprobe techniques. Thus, it was not possible to attribute the observed stress corrosion to intrinsic behavior. The fact that the slope of the curve was further influenced by the presence of DMF suggested the existence of a mechanical mechanism for crack extension although this view was not completely consistent with the apparent effect of varying specimen chemistry.

The earlier work left several important questions unanswered as well as a clear conclusion over the dominant mechanism. These questions were:

- . What was the difference in chemical corrosion of MgO by DMF compared with H_2O and on H_2O versus the ambient air during a dynamic strength test?
- . Would MgO, which was free of grain boundary phase, behave quite differently?
- . Would the stress corrosion of MgO in H_2O be influenced by a 1-hour hold under no load?
- . Would the corrosion curves be substantiated with increased numbers of tests?

B. Material and Procedure

1. Specimen Preparation

Early work had established the difficulty in producing high purity dense MgO with uniform fine-grain microstructures. (12) Secondary grain growth led to a marked duplex structure in specimens produced from calcined 99.9995% $\text{Mg}(\text{OH})_2$. The solution to this microstructure development problem was the subject of a concurrent program, (29) and this development was not sufficiently advanced to supply material to the present study. A limited effort was generated in this program to fabricate suitable specimens from the following powders:

- . J.T. Baker, Ultrex grade, 99.96% MgO
- . Johnson-Matthey, High purity grade, 99.999% MgO

The results were decidedly unrewarding as only 97% density was achieved in the six pressings conducted, and the specimens possessed a marked duplex structure.

It was reported (30) that the sintered MgO produced by Honeywell and used by other investigators (31,32) was of moderately high purity ($\sim 99.95\%$ MgO), single phase, quite dense ($\geq 99.3\%$), and possessed a uniform $43 \mu\text{m}$ grain size. Three slabs which had been processed together were purchased and machined into $0.050 \times 0.100 \times 1.125$ test specimens. A typical microstructure

is shown in Figure 9 which tends to confirm the expected properties. However, it was possible to find isolated second phase fields (arrow). Also, examination by replica techniques revealed some grain boundaries which definitely had width and apparent second phase, (Figure 10). Nevertheless, testing was conducted on this material with the view that it was not yet within the "state-of-the-art" to produce cleaner MgO having the listed desired properties and testing of this material would answer most of the questions concerning stress corrosion in MgO.

2. Sample and Test and Environment Arrangement

The dead-load fracture tests were conducted in 4-point bending in two lever arm test frames equipped with microswitch-cloth arrangements to record time to failure. A brass 4-point bend test fixture was equipped for holding liquids, and tungsten (outer) and alumina (inner) knife edges were employed on one piece of apparatus and sapphire knife edges were employed in the second apparatus which also had high density graphite exposed to the environment. Mylar sheet was inserted between the knife edge and the specimen.

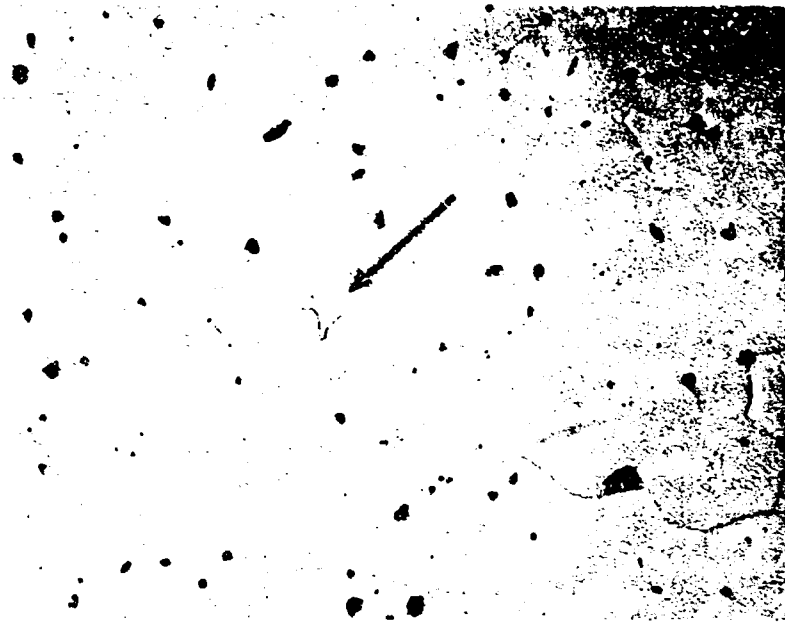
Base-line dry strength was obtained by heating the specimen to 900°C in argon to desorb H₂O, holding for 1 hour, cooling to 23°C and loading to fracture at a constant load rate approaching 4×10^{-5} /sec strain rate without breaking the test atmosphere.

Three different discs were sectioned into specimens. The test plan was organized such that a near equal number of test bars were included from each disc for each test condition. This plan was formulated only after the initial dynamic tests indicated that the specimens could be treated as one population strength group.

Dynamic strength tests were also performed in the various test environments, H₂O, DMF and DMSO-10% DMF. The (CH₃)₂SO + 10 v/o (CH₃)₂NCHC, DMSO-DMF solution was chosen as an additional test environment as it had been shown by Westwood^(25,26) to exhibit a minimum in the MgO dislocation mobility in the composition field between DMSO-DMF. It is expected that this minimum would occur at a slightly different DMSO-DMF composition for MgO using a different impurity composition (defect structure) than that tested by Westwood. However, it is argued that the dislocation mobility would be markedly reduced over pure DMF and would offer a related chemical environment to aid in separating potential chemical corrosion effects. Measurements in this media would be comparable to those in H₂O insofar as dislocation mobility was concerned. All tests were performed after immersion for 1 hour since a question concerning the effect of such a hold remained after the previous stress corrosion tests in H₂O where no hold was involved.^(11,12)

3. Results

The dynamic strength results are given in Table II. Examination of the data shows that testing in all three liquid medias gave average strength values within the standard deviation range of the average dry strength. It is interesting that all the average strengths were lower in the liquid media, but there is no valid reason to conclude from this



#5427-3

500X

Figure 9. Typical Microstructure of Sintered MgO Showing Overall Single Phase Material, some Porosity and Second Phase Patches.



#71029

7500X

Figure 10. Fractograph Showing Apparent Grain Boundary Phase in Sintered MgO.

evidence that this reflects an action of the liquid media on the strength limiting flaw. These tests indicate that the organic fluids certainly are not strongly chemically corrosive to MgO.

TABLE II
DYNAMIC ROOM TEMPERATURE STRENGTH OF SINTERED MgO

<u>Test Environment</u>	<u>No. of Tests</u>	<u>Average Bend Strength, Kpsi</u>	<u>Standard Deviation Kpsi</u>
Argon after 900°C heat treatment	6	27.9	± 3.8
H ₂ O	3	24.9	-
DMF	3	25.3	-
DMSO-10%DMF	3	27.1	-

The delayed fracture results are reported in Table III. Seven of the test specimens fractured during loading and these were not plotted in the graphs which follow. It is not clear why all of these specimens failed under loading, but in one case an obvious microscopic flaw was located (Figure 11). It is suspected that other specimens in this category may have contained less obvious large (compared with the grain size) flaws. This same comment applies to the low end of the strength curve for the dynamic tests. Specimens which were being loaded to high fractions of their dry strength undoubtedly failed because they were undergoing short-term stress corrosion. It is well known that stress corrosion effect can be seen in glass at times $< 10^{-2}$ sec.

The data for the H₂O, DMF and DMSO-10DMF test media are plotted in Figures 12, 13, 14, respectively. The points highlighted with an arrow indicate that the test was terminated at that point in time without fracture, or in the case of Figure 14, that a specimen was still under test at the time this report was written. The approximate least square lines were estimated. Fracture features were examined by electron microscopy replica techniques. Two samples tested in H₂O were examined in detail. Figure 15 illustrates several fracture features which were typical of those found near the tensile surface. These include a pock-marked corroded surface, A, several secondary cracks with branches, B, and curved river mark steps on a single fracture face. This fractograph was from Sample DQ6-8 which experienced a relatively short (230 sec) load to fracture. Sample DQ3-6 fractured after 12×10^7 sec and contained the same curved ledges plus cube or diamond shaped pits as illustrated in Figure 16a. This sample was removed from the H₂O within several minutes of fracture, thus these features most probably were not caused by corrosion after fracture had occurred. Many of the pits are associated with ridges. One interpretation is that the crack front progressed successively to the various pit lines and the pit formation was caused by a stress enhanced chemical corrosion

TABLE III

DELAYED FRACTURE TESTS ON SINTERED MgO

<u>Specimen</u>	<u>Environment</u>	<u>Load Kpsi</u>	<u>σ/σ_D</u>	<u>Time to Failure, sec</u>
DQ6-13	H ₂ O	23.8	0.851	2.4×10^1
DQ3-7	H ₂ O	22.4	0.802	0
DQ6-8	H ₂ O	22.4	0.802	2.29×10^2
DQ6-6	H ₂ O	22.4	0.802	Still running at 1.86×10^4
DQ3-8	H ₂ O	21.0	0.754	1.58×10^2
DQ5-10	H ₂ O	21.0	0.754	4.64×10^3
DQ3-6	H ₂ O	19.6	0.703	1.18×10^6
DQ6-7	H ₂ O	18.2	0.654	0
DQ5-7	H ₂ O	15.4	0.552	Still running at 3.59×10^5
DQ6-10	DMF	23.8	0.851	0
DQ6-11	DMF	23.8	0.851	7.4×10^1
DQ6-9	DMF	22.4	0.802	2.67×10^2
DQ5-8	DMF	22.4	0.802	3.60×10^2
DQ3-9	DMF	21.0	0.754	8.5×10^5
DQ5-9	DMF	21.0	0.754	Still running at 9.2×10^5
DQ5-12	1M DMF	22.4	0.802	0
DQ3-12	1M DMF	21.6	0.773	0
DQ5-13	1M DMF	21.0	0.754	7.09×10^3
DQ6-14	DMSO-10% DMF	23.8	0.851	7.69×10^2
DQ3-10	DMSO-10% DMF	23.8	0.851	0
DQ5-7	DMSO-10% DMF	23.8	0.851	4.46×10^2
DQ3-11	DMSO-10% DMF	22.4	0.802	0
DQ5-11	DMSO-10% DMF	22.4	0.802	4.81×10^1
DQ3-13	DMSO-10% DMF	22.4	0.802	2.12×10^5
DQ5-14	DMSO-10% DMF	21.6	0.773	1.81×10^6
DQ6-12	DMSO-10% DMF	21.0	0.754	Still running at 4.8×10^6
DQ5-7	DMSO-10% DMF	19.6	0.703	Still running at 2.3×10^6



#5427-1

100X

Figure 11. Flaw Located at Fracture Interface of Sintered MgO (A - plastic mount, B - flaw, C - MgO Matrix).

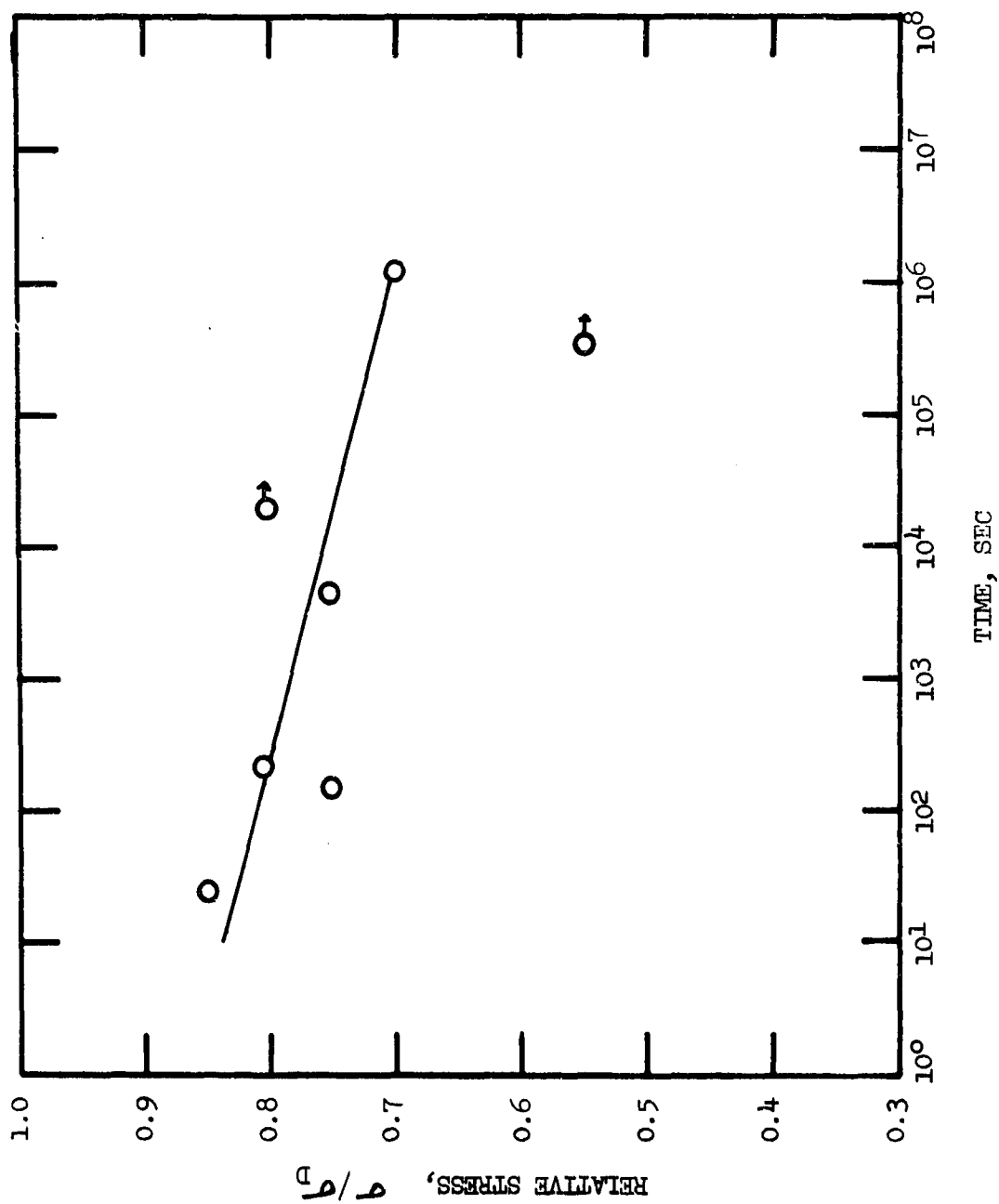


Figure 12. Delayed Failure Curve for Honeywell Sintered MgO Tested in Distilled H₂O.

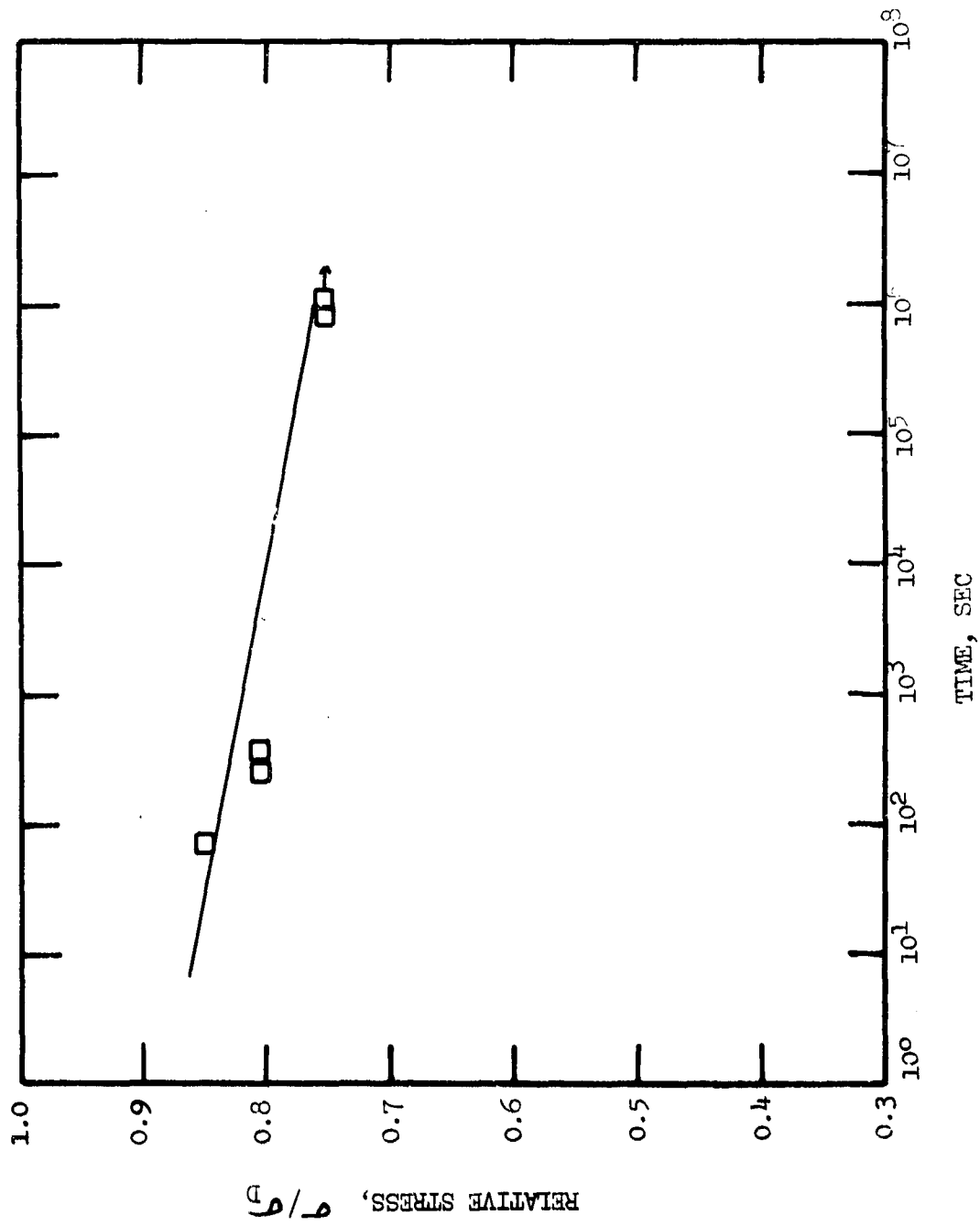


Figure 13. Delayed Failure Curve for Honeywell Sintered MgO Tested in DMF.

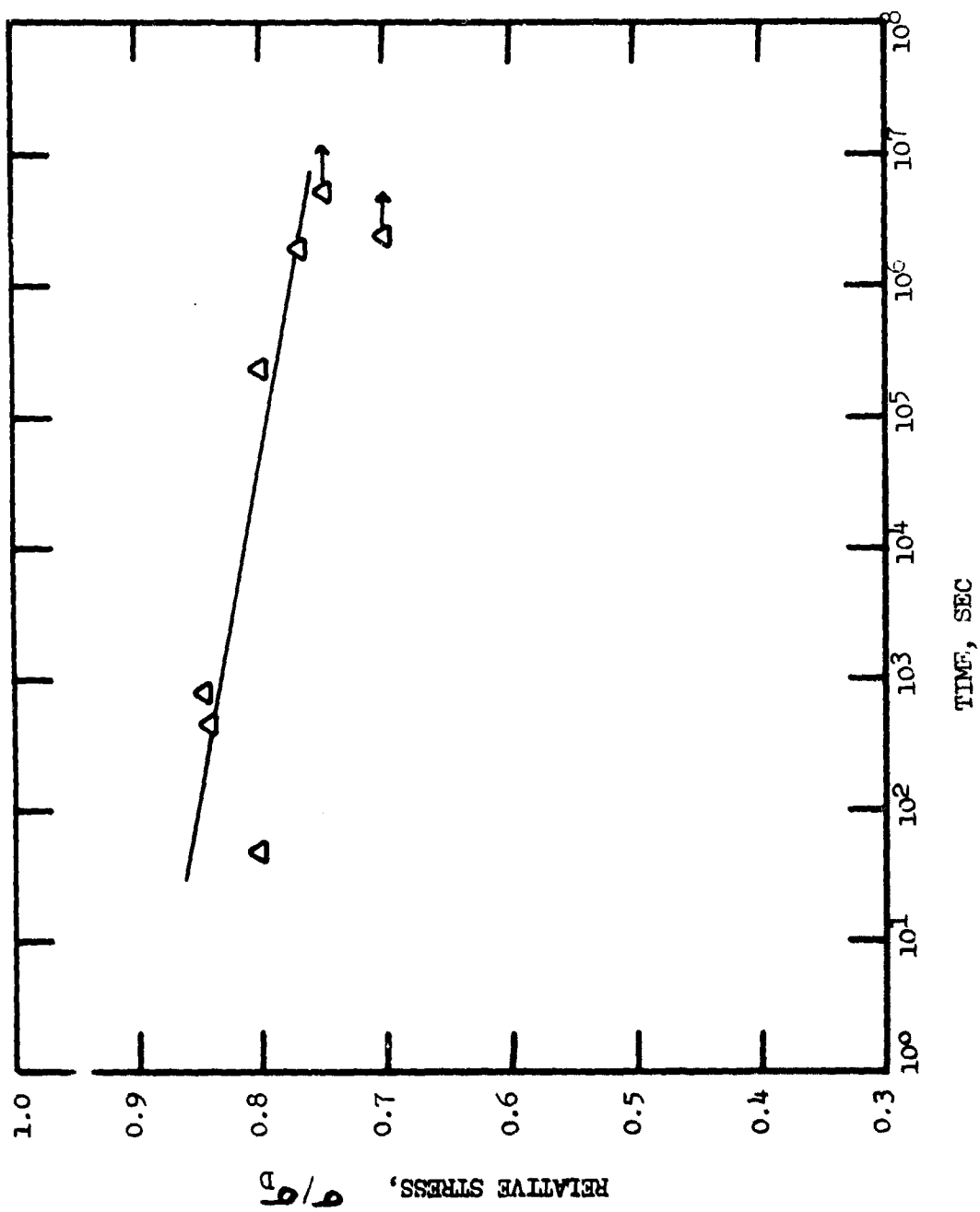


Figure 14. Delayed Failure Curve for Honeywell Sintered MgO tested in DMSO-10 v/o DMF.



#71018

7500X

Figure 15. Fractograph of Static Fatigue Specimen Tested in H_2O Exhibiting (A) Corroded Surface, (B) Secondary Cracks, (C) River Marks.



#71027

(a)

7500X



#71028

(b)

7500X

Figure 16. Fractograph of Static Fatigue Specimen Tested in H_2O Exhibiting, (a) Pits Associated with Crack Arrest Lines and, (b) Random Flat Bottom Pits on Grain Face.

perhaps at point defect centers. A variation of this interpretation would again associate the pits with a crack arrest position, but that the pits reflected the existence of a dislocation line. The fact that the pits are flat-bottomed argues against a dislocation model although a mobile dislocation could have left the sight of the pit formation and the pit bottom could flatten by subsequent corrosion. However, as shown in Figure 16b areas were found which not reflect the symmetry usually associated with slip bands and dislocation activity, thus the pit appear to reflect a chemical rather than a mechanical process. Sample DQ3-9 was tested in DMF and exhibited evidence for secondary cracks radiating from pores, Figure 17. However, there were no other distinguished features within the field of view examined.

Fracture surfaces were also examined for the specimens tested dynamically both dry and in the various liquid media. This served as a basis for comparison with features found on the delayed fracture specimens. Examination of specimen DQ5-5 tested in argon, Figure 18, revealed secondary cracks, (A), a textured grain face, (B), cleavage steps, (C), and a river pattern (D). Dynamic tests in all three liquid media also exhibited these features. No other distinguishing fracture features were found, however.

4. Discussion

The stress corrosion data for the three grades of MgO tested in the last three years are plotted in Figure 19. Consider first the lines for the three grades of MgO tested in one environment - water.

The lines A, B and C are quite different both in slope and height. The trend did not correlate with any microstructural feature such as grain size or porosity. This suggests that the behavior is related to an extrinsic chemical effect. In all three cases microstructural evidence was presented for the existence of minor amounts of grain boundary phases. Since the starting materials and processes by which the three types of MgO were fabricated were quite different, it is very probable that the composition of the second phases was quite different. Only in the case of the Fisher MgO has the second phase been identified, and a $\text{Na}_6\text{Al}_4\text{Si}_4\text{O}_{17}$ compound was found by electron diffraction techniques in this case. Other investigators^(27,28) have observed Si and Ca segregation at grain boundaries in hot pressed MgO somewhat similar to the Fisher or Baker MgO tested in this program. The Honeywell sintered MgO was undoubtedly the purest material tested, thus it would be reasonable to expect this to have a quite different second phase chemistry and different extrinsic stress corrosion. It is difficult to develop an argument based on a mechanical corrosion model consistent with the data. However, it does appear reasonable that chemical stress corrosion, especially if it was extrinsic, would vary considerably with starting powder and method of fabrication.

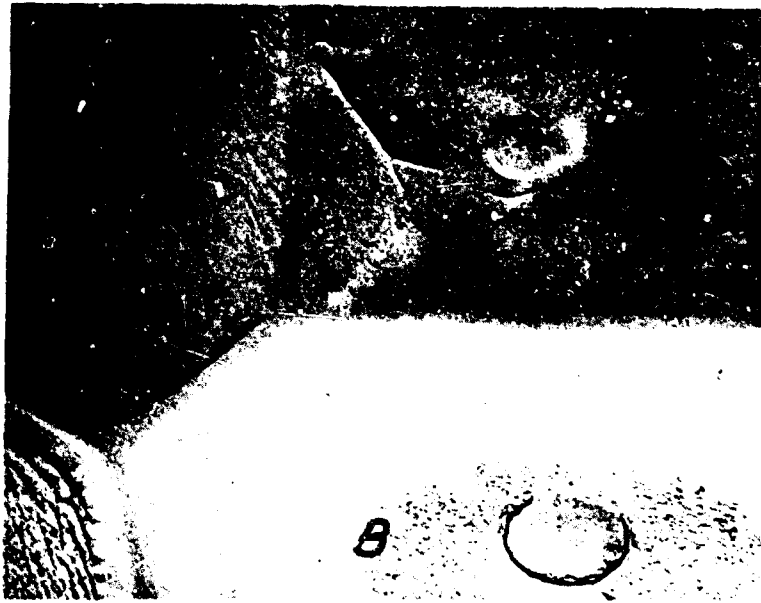
A comparison of the varying environment stress corrosion curves. C, E and F for sintered MgO lends additional insight into the mechanism. The analysis was subject to possible error due to scatter in the data; however, the authors believe that the trends make it possible to draw valid conclusions. Both curves E and F in the DMF and the DMSO-10% DMF environments, respectively, lie above curve C for the H_2O environment. Westwood⁽²⁶⁾



#71063

4500X

Figure 17. Fractograph of Static Fatigue Specimen Tested in DMF Showing Secondary Crack Associated with Pores.



#71048

(a)

7500X



#71047

(b)

7500X

Figure 18a and b. Fractograph of Dynamically Argon Pested MgO Showing, (A) Secondary Cracks, (B) Textured Grain Face, (C) Cleavage Steps and (D) River Pattern.

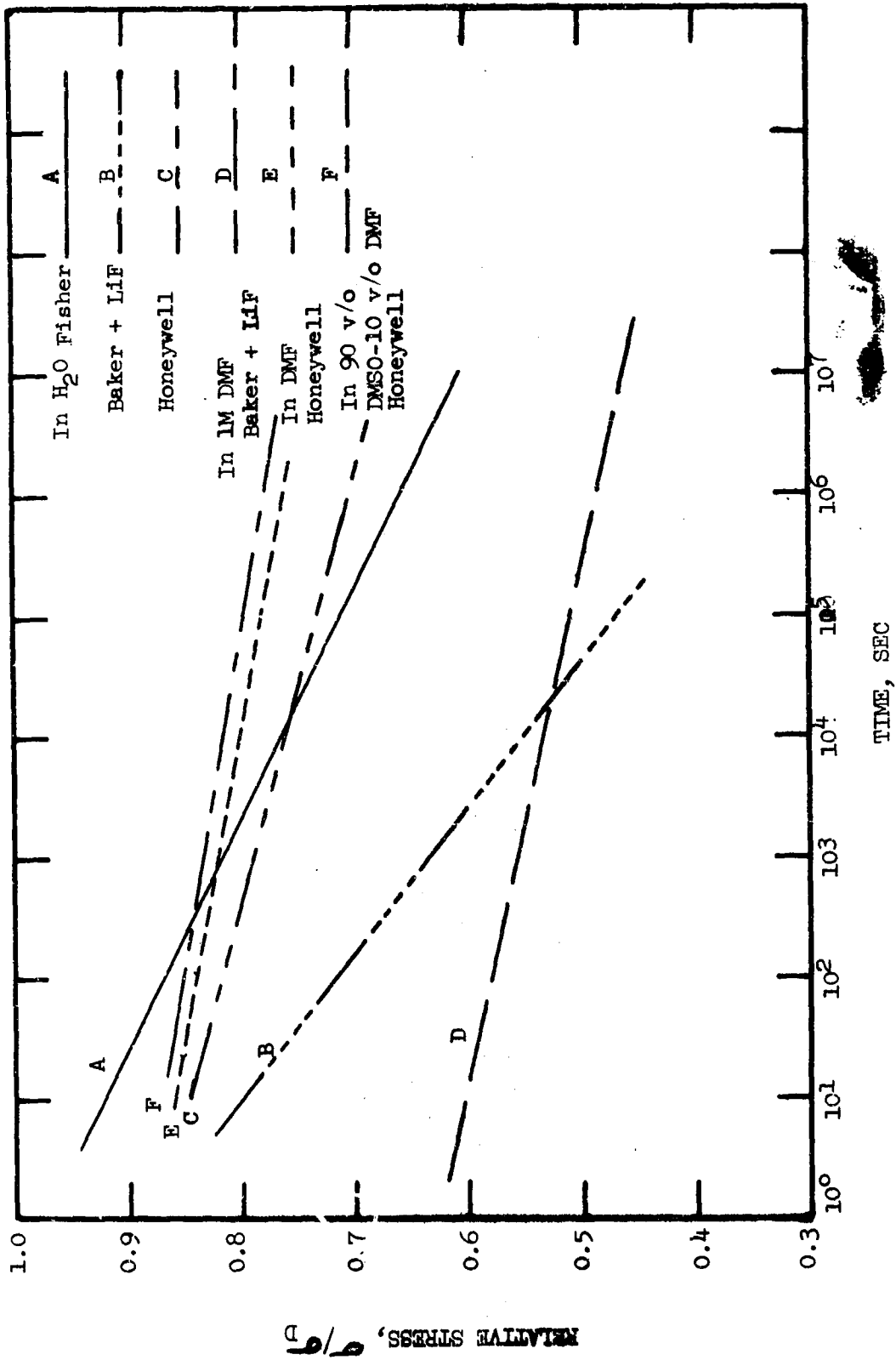


Figure 19. Delayed Failure Curves for Two Hot Pressed and One Sintered Grade MgO in Four Test Environments.

showed that for Norton single crystal MgO pure H₂O and DMSO-10 DMF exhibited nearly identical dislocation velocities. Thus, it would appear that in the absence of H₂O the stress corrosion resistance has been improved by some mechanism other than a mechanism strictly dependent on dislocation velocities. However, there is a distinct difference in the stress corrosion behavior in the DMF and DMSO-10% DMF solutions. The environment in which the dislocation velocity was expected to be the lowest (DMSO-10% DMF curve F) did result in the most corrosion resistant environment. Taking this curve as a base-line the adsorption of DMF molecules apparently result in a distinctly lower resistance to stress corrosion, presumably due to the increased dislocation velocity and its effect on crack propagation.

The lowest stress corrosion resistance was exhibited by Baker (by the LiF process) in 1 molar dimethyl formamide (in H₂O). During this period several similar tests were conducted using the Honeywell MgO (Table III). The extremely low stress resistance shown for the Baker MgO was not confirmed in the recent tests although only one specimen gave a delayed fracture result. The marked reduction in load bearing capability may have been due to a combined stress enhanced chemical dissolution tied in with increased dislocation mobility in some rather complicated way. It is unclear why this curve should cross the curve for H₂O in this material with this mechanism operating, however. Clearly, the 1M DMF environment gives the most complicated behavior.

The fractographic study revealed only one type of feature that could be identified as having been caused by stress corrosion. This was the flat-bottom pits associated with steps on a fractured grain face found in a long term H₂O test specimen (Figure 16). All the other features such as river marks, secondary cracks, etc., could be found in dynamic dry test specimens. The pits are interpreted to be caused by stress enhanced chemical dissolution. The most convincing evidence is shown in Figure 16a where this corrosion was apparently associated with crack arrest lines which, of course, would be lines of high stress enhancement. Thus, the fractographic study supported a chemical corrosion model for the H₂O tests. The fractographic study neither refuted or reinforced arguments for a mechanical dislocation model of stress corrosion in DMF and DMSO-10% DMF.

C. Summary and Conclusions

1. Stress corrosion studies in a H₂O environment on two hot pressed grades and one sintered grade of polycrystalline MgO demonstrated that the behavior was extrinsic and probably related to grain boundary impurities rather than lattice impurities. Electron microscopic examination revealed thin grain boundary second phases in all three materials and in one case a Na₆Al₄Si₄O₁₇ grain boundary phase was identified. Further fractograph studies revealed flat bottom pits associated with crack arrest lines.
2. Testing in DMF and DMSO-10% DMF solutions where DMF enhances dislocation velocities over the other organic solutions and H₂O revealed measurable differences with increasing stress corrosion resistance in the order H₂O,

DMF, and DMSO-10% DMF. Fractographic studies of the DMF or DMSO-10% DMF test bars did not reveal any unique features.

3. It is concluded that in the presence of H₂O stress corrosion is dominated by a chemical corrosion process that varies with the grain boundary chemistry of the MgO body. In the absence of H₂O dislocations play a role in the stress corrosion process that is probably more related to the MgO microstructure than the presence of minor grain boundary phases. It is expected that truly single phase MgO would not be as sensitive to stress corrosion by H₂O and may, in fact, be controlled by a mechanical dislocation stress corrosion mechanism in all of the environments discussed.

IV. PRESS FORGING ALUMINA HEMISPHERES

A. General

There are at least three potential motivations for forging Al₂O₃. They are, 1) the production of complicated shapes where a fine grain dense microstructure is required, 2) improved mechanical properties due to the texture and retardation of structure sensitive failure mechanisms, and 3) high in-line optical transmission due to the crystallographic texture and the elimination of light scattering from birefringence. During this report period, the experimental effort has been concerned with producing a material that would take advantage of all three potential benefits of press forging. The goal was to fabricate high strength transparent alumina hemispheres.

Serious consideration of press forging alumina began when it was discovered that alumina single crystals were grown as a result of press forging by an apparent strain anneal technique.⁽³³⁾ This was followed by the development of alumina with high in-line transmission due to the absence of porosity together with a strong preferred crystallographic texture.⁽³⁴⁾ The subsequent work^(35,36,11,12,13) revealed that deformation-recrystallization processes usually associated with metal working practice were responsible for the structures and properties observed. The deformation process itself produced a highly elongated grain structure with the long axis of the grains normal to the pressing direction. This was due to the dominance of basal slip. Upon primary recrystallization the microstructural texture was often destroyed, the the basal crystallographic texture which had accompanied the grain texture was retained. Also accompanying primary recrystallization and the equiaxed microstructure resulting from the process was a pore removal mechanism. It was suggested⁽³⁵⁾ that the porosity distributed throughout the structure presented preferred nucleation sites for the new generation of grains. This process itself could absorb porosity or the structure could be more susceptible to continued densification due to the nearness of pores to grain boundaries; their potential sink.

Improved in-line transmission was the most dramatic outcome of the forging effort.⁽³⁴⁾ In-line light transmissions of 60% were achieved for the forged material as compared with a maximum of 20% for the best randomly

oriented pore-free Al_2O_3 available at an equivalent thickness. This resulted from the preferred basal texture eliminating to a large extent the light diffraction due to birefringence. Inverse pole figures demonstrated that the crystallographic orientation was not perfect which undoubtedly accounted for the absence of even higher optical transmission figures.

The mechanical properties have been studied extensively,⁽¹²⁾ and it was found that the strength at -196°C and 1200°C was nearly independent of grain size in the 1-20 micron range. Fracture strengths in the 1200 to 1475°C range were over 50% higher than straight hot pressed material of an equivalent grain size.⁽³⁶⁾ However, there was no apparent effect of texture on the plastic properties between 1475 - 1700°C .⁽¹³⁾

A limited effort was centered on deep drawing high density (99%+), 2 μ grain size, hot pressed discs. A number of 60° cones were fabricated and several were completely free of cracks with the cone tip being the most sensitive area. The others possessed a small amount of cracking in this region. A full hemisphere was forged, but it cracked into several pieces due to cooling contraction on the male punch. Recently, a sound hemisphere was formed on a related program.⁽³⁾

With this background, it was decided to fabricate a specimen with all of these desirable properties; a transparent strong Al_2O_3 hemisphere. This required combining the best engineering approaches tried up to that point in time. For example, the most transparent specimens were fabricated by the powder forging technique (a cold pressed preform was placed in the die and allowed to sinter and shrink prior to reaching the forging temperature and the initial ram deflection). Previous shape drawing had only been accomplished using a hot pressed dense disc of equal or larger diameter than the final cone or hemisphere. The combined approach consisted of starting with undersized cold pressed or cold pressed and presintered preforms placed in a hemispherical die as illustrated in Figure 20. The forging process then consisted of height reduction accompanied by lateral expansion, back extrusion and densification.

B. Material and Procedure

1. Raw Material

The base starting powders were 99.9+% pure Al_2O_3 from two sources:

1. Code M-1, A. Meller Co., Providence, R.I., 0.3 micron Al_2O_3 , mainly alpha but containing 10-20% gamma Al_2O_3 ,
2. Code AM-7, AM-8, experimental powder from W.R. Grace Co., Clarksville, Md., 0.2 micron alpha Al_2O_3 containing 0.1% MgO.

The W.R. Grace powder was used in the "as received" or dry ball milled form. An addition of 0.2 wt. % MgO was made to the A. Meller powder by standard wet milling techniques.

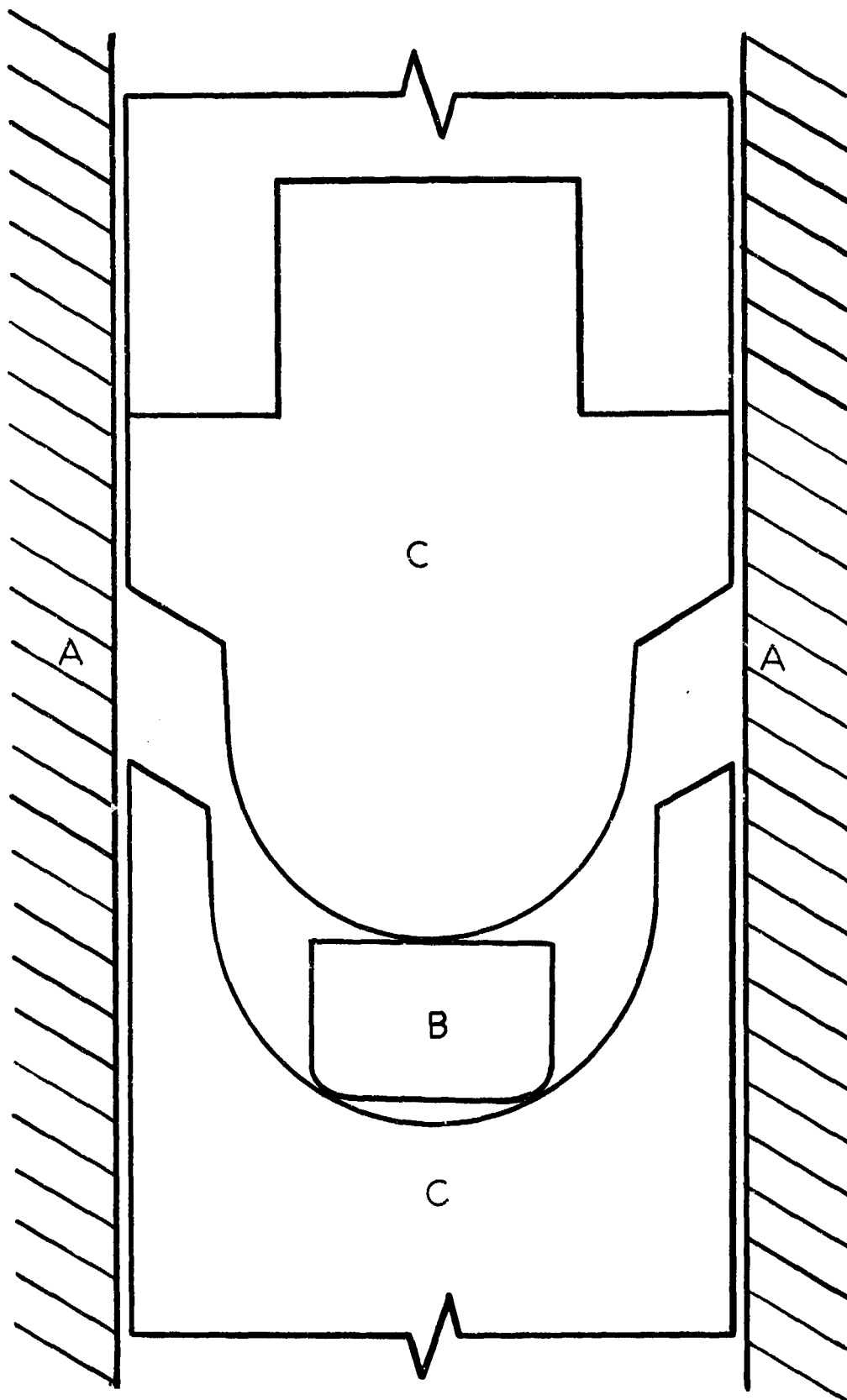


Figure 20. Sectional View of Die (A), Al_2O_3 Preform (B) and Male and Female Punch (C).

2. Forging Apparatus

A conventional induction heated graphite hot pressing furnace and press were utilized. ATJ graphite outer die, hemispherical die and punches were utilized for the initial runs. Later a hemispherical die was fabricated from high strength (18,000 psi tensile strength) Poco graphite.

A pinned top ATJ punch was used which allowed hot extraction of the male die. This was thought necessary because of the fracture of an early hemisphere presumably due to cooling contraction on the male punch. The boron nitride die lubricant was sprayed directly onto graphite. Previously molybdenum foil separated the graphite and BN. Foils were not practical because of the geometry although plasma spraying a Mo layer could be attempted although inferior performance would be expected due to residual porosity. Ambient atmosphere forgings were employed which meant that at the forging temperature it was predominantly CO with a partial pressure of CO₂ and A. The argon permeated into the cavity from the sight tube where it was employed as a sight tube flush. Also, residual nitrogen was expected.

3. Procedure

After loading the cold pressed or sintered disc into the die cavity and assembling the furnace, the die was heated to the forging temperature on a schedule which was slow (2-3 hours) if a cold pressed preform was utilized and fast (1/2-1 hour) if a presintered preform was used. Upon equilibrating at temperature, the ram travel was initiated and driven by a manual strain rate control. A typical deflection-pressure curve is illustrated in Figure 21. The strain rate during the rapid deflection regime was controlled to between $6 \times 10^{-4} \text{ sec}^{-1}$ and $1 \times 10^{-3} \text{ sec}^{-1}$. Studies under a separate program⁽³⁾ are concerned with strain rate and strain criteria for achieving highly deformed crack-free Al₂O₃. The above strain rates are the best present estimates of acceptable strain rates in the 1850°C range. Once maximum pressure is reached the deflection rate slows down as forging and densification come to a conclusion. The specimen is usually held at maximum temperature and pressure for some prescribed period of time beyond that where deflection has apparently ceased. Some densification continues by diffusion, and there is some evidence that multiple recrystallizations may take place in this period,⁽³⁵⁾ thus, a hold of 3-4 hours has become standard practice. Upon completion of the run, pressure is released and the male punch extracted. It is at this point that the temperature is allowed to drop.

4. Analysis

In a hot working study it is a necessity to have some technique for determining preferred orientation and degree of texture. This is best accomplished by x-ray diffraction techniques. A technique was described⁽³⁷⁾ which is not as tedious as the construction of a pole figure, but which allows the evaluation of relative degrees of orientation. The diffraction pattern of a random (powder) sample was obtained. Values of $f_0(h,k,l)$ defined by the relation

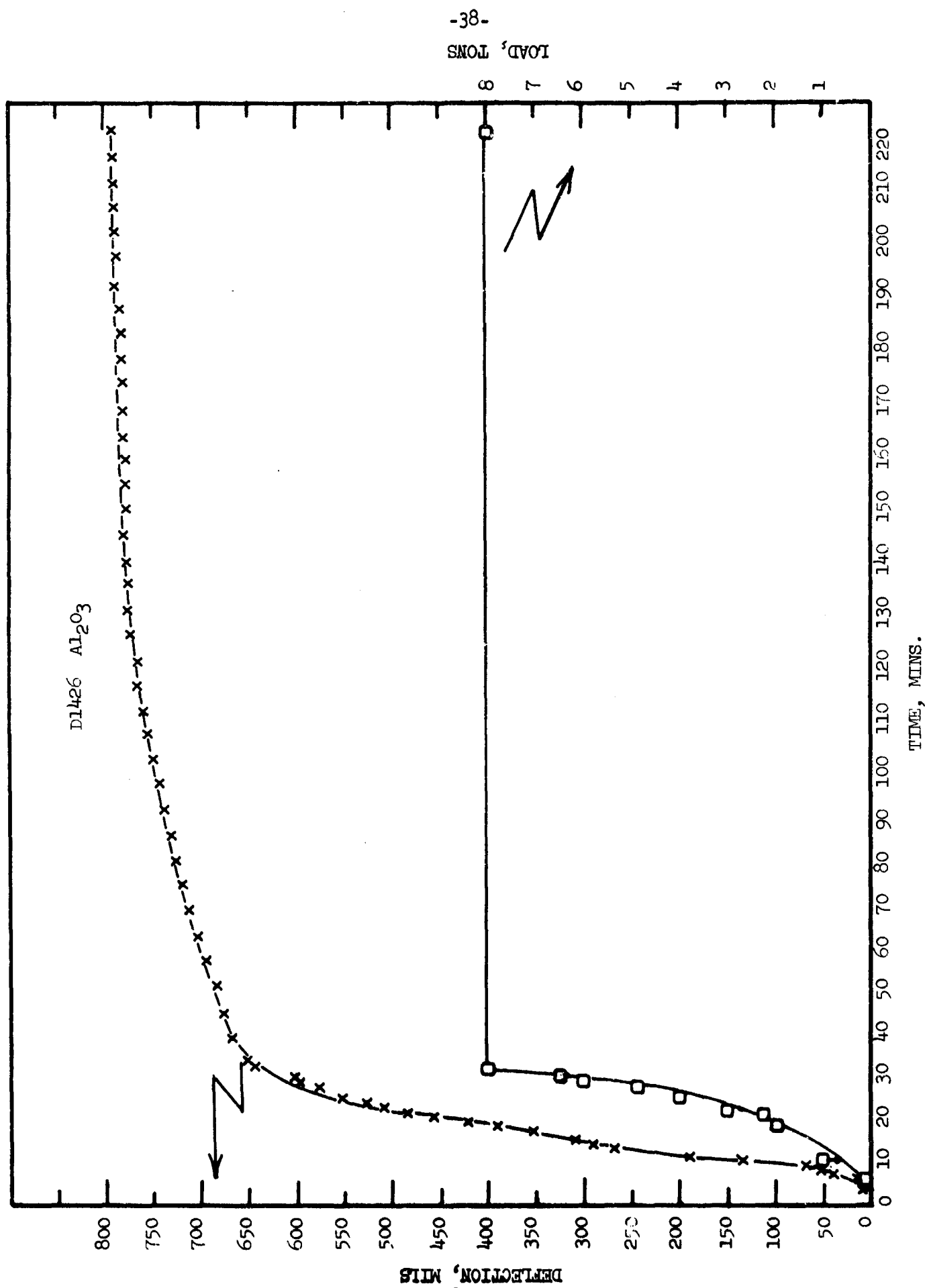


Figure 21. Record of Deflection and Pressure Versus Time in a Typical Hemisphere Forging Run.

$$f_o(h,k,l) = \frac{I(h,k,l)}{\sum_{hkl} I(hkl)}$$

were calculated. Similarly, values $f(hkl)$ were calculated from the diffraction pattern of a forged specimen. The ratios $R(hkl) = \frac{f(hkl)}{f_o(hkl)}$

which give the relative intensity of reflection were calculated against the angle ϕ between the planes (hkl) and the basal plane. In the case of a random (powder) sample, R has the constant value of unity. In the case of a perfectly oriented sample, R is zero everywhere except at $\phi = 0$ where it has some large finite value. In the case of a distribution of orientation, in general, R will decrease monotonically from $\phi = 0$ to $\phi = 90^\circ$. The better the crystallites are aligned, the higher the intercept at $\phi = 0$ and the steeper the drop with increasing ϕ .

C. Results and Discussion

Two introductory forgings were conducted with cold pressed AM-8 powder. These samples as well as the other hemispherical forgings conducted during this period are listed in Table IV. A photograph of the initial hemispherical forging is shown in Figure 22. Both of these initial samples were very translucent in a central zone occupying about 2/3 of the arc. Tearing occurred at the rim of the sample in a low density zone occupying the remainder of the sample. The central zone of each sample contained several healed cracks; an example is shown in Figure 23. It was thought that cracking occurred early in the preform sintering or forging process allowing BN intrusion, reaction, bonding and healing. Microhardness indentations on the second phase revealed an average hardness of 1420 Knoop as compared with 1710 Knoop for the α Al_2O_3 matrix. This intermediate hardness value indicates that the BN had in fact reacted with the Al_2O_3 to form a new phase. The phase identification was not pursued further.

A series of experiments were conducted to establish conditions for preparing preforms that would not develop cracks up to the point at which forging commenced. These experiments are listed in Table V. Basically, a series of cold pressed discs or long cylinders were prepared. Next, they were cut and shaped into the geometry shown in Figure 20. Finally, they were cycled through the first part of the normal forging sequence - up to the point where pressure was applied, cooled and examined for the presence of cracks. Two types of defects were noted; surface cracks as shown in Figure 24a and agglomerate shrinkage cracks as shown in Figure 24b. Also, Sample 1452D exhibited evidence for preferred agglomerate sintering which was attributed to the fact that dry ball milled powder was employed. Crack-free preforms were fabricated by isostatically pressing a $1\frac{1}{2}$ -inch diameter by 3-inch long cylinder and using just the bottom end. The closure apparently sets up strains during pressing that develop into cracks during sintering. Dry cutting with a SiC cut-off wheel and hand dressing with SiC paper appears to be a satisfactory operation for the purpose of achieving the proper geometry.

Several problems were uncovered that were not originally suspected. The thermal cycle employed in sintering the preform during heating to the

TABLE IV

HEMISPHERICAL FORGING EXPERIMENTS

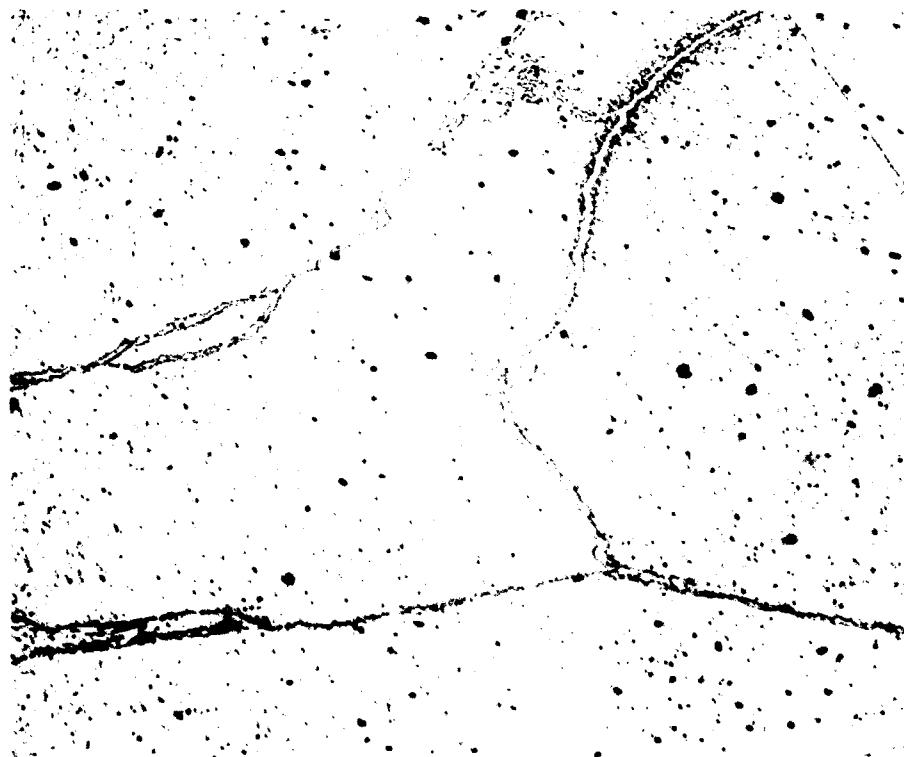
Experiment	Powder Lot	Preform Prep.	Preform Density gm/cc	Separating Media	Temp. °C (corrected)	Pressure Kpsi	Time min.	Density gm/cc	Remarks
1426	AM-8	Cold press 40 Kpsi	2.0	BN	1925	5.1	215	3.90	Central 2/3 of arc translucent, healed cracks at center, tears at edge
1432	AM-8	Cold press 40 Kpsi	2.0	BN	1925	5.1	195	3.95 (center)	Central 2/3 of arc translucent. Four cracks transmitted to crown, edge tears
1456	AM-8	Cold press 40 Kpsi	2.0	BN	1925+	5.1	99	-	Melt out $\frac{1}{2}$ O ₂
1486	AM-8	Cold press Sinter H ₂	3.90	HTP-BN	1850	5.1	225	3.74	Transparent edges, slightly porous center and rim, micro-cracks
1493	M1 0.2 MgO	Cold press sinter	3.70	HTP-BN	1850-1880	6.4	210	3.84 3.98 (center)	Central 2/3 of arc translucent - porous rim, micro-cracks
1497	M1 0.2 MgO	Cold press	3.90	Dylon, BN	1855-1875	8.3	42	3 76	Forging terminated early due to punch failure, 1/3 of cross-section translucent



#5300-2

1 1/2X

Figure 22. Initial Al_2O_3 Hemisphere Forged from Powder.



#5327-7

50X

Figure 23. Cross-Section of Hemispherical Forging D1432
Showing Second Phase Intrusions into Cracks.

TABLE V

PREFORM PREPARATION AND RESULTS AFTER SHORT SINTER

Experiment	Powder Lot	Green Pressing Condition	Post-Pressing Treatment	Position of Pressure Train	Fired Density	Condition of Fired Sample
D1446*	Grace AM 8	Isostatic - 40 Kpsi	Dressed on belt sander	Resting on	93.8	Small cracks where punch was resting. Also, agglomerate shrinkage cracks.
D1449*	Grace AM 8	Isostatic - 40 Kpsi	Dressed on belt sander	No pressure	97.1	Small cracks but more open on top. Also, agglomerate shrinkage cracks.
D1452A*	Grace AM 8	Section next to closure on 3" long Isostatic - 40 Kpsi	Presintered 1100°C 2 hrs., dressed on belt sander	No pressure	89.8	Small open cracks on top. Also, agglomerate shrinkage cracks.
D1452B*	Grace AM 8	Middle section of 3" long Iso - 40 Kpsi	Cut on band saw only	No pressure	-	No surface cracks, but delaminated in middle.
D1452C*	Grace AM 8	Bottom section of 3' long Iso - 40 Kpsi	Cut on band saw and dressed on belt sander	No pressure	86.2	Several small cracks on periphery.
D1452D*	Grace Dry Ball Milled AM 7	Uniaxial press 15 Kpsi	Presintered 750°C 2 hrs. Dressed on belt sander	No pressure	75.5	Several open cracks on periphery.
D1452E*	Grace AM 8	Isostatic - 40 Kpsi	Dressed on belt sander	No pressure	-	Small open cracks on top and sides.
1473 A*	M1 + 0.2% MgO	Isostatic 40 Kpsi	Cut on SIC wheel-hand dressed	No pressure	95.3	Sound, no surface cracks or defects

TABLE V (Concl'd)

PREFORM PREPARATION AND RESULTS AFTER SHORT SINTER

Experiment	Powder Lot	Green Pressing Condition	Post-Pressing Treatment	Position of Pressure Train	Fired Density	Condition of Fired Sample
1473 B*	Grace AM 8	Isostatic - 40 Kpsi	Cut on S1C wheel - hand dressed	No pressure	94.2	Cracked into 4 pieces
1479*	MI + 0.2% MgO	Isostatic - 40 Kpsi	Cut on S1C wheel - hand dressed	No pressure	-	Melted
1481 A*	MI + 0.2% MgO	Isostatic - 40 Kpsi	Cut with saw - hand dressed	No pressure		Slight reaction
1431 B*	MI + 0.2% MgO	Isostatic - 40 Kpsi	Cut with saw - hand dressed	No pressure	89.5	Sound
1481 C*	MI + 0.2% MgO	Isostatic - 40 Kpsi	Cut with saw - hand dressed	No pressure		Sound
1483**	MI + 0.2% MgO	Isostatic - 40 Kpsi	Cut with saw -	No pressure	92.8	Sound

* Samples fired at 1925°C for 5 minutes (experiment 1481 held for 60 minutes for temperature experiments).

** Sample fired at 1855°C for 5 minutes.



#5327-3

(a)

3X



#5397-2

(b)

100X

Figure 24. Defects Noted in Early Al_2O_3 Preforms; (a) Surface Cracks and (b) Internal Agglomerate Shrinkage, Cracks.

forging temperature develops a high density skin approximately 1/8-inch thick. Also, run 1483 exhibited a second phase which has not been unequivocally identified. X-ray studies showed that Al_2O_3 -rich MgAl_2O_4 or $\text{Al}(8/3 + x/3)\text{O}_{4-x}\text{N}_x$ were possible identifications. From the standpoint of reactants, either phase was possible; however, the presence of MgAl_2O_4 would be surprising at the 0.2% MgO level. It is thought that 0.2% MgO is within the Al_2O_3 solid solution phase field.⁽³⁸⁾ It is possible, of course, that vapor phase transport concentrated MgO in the outer layer of the compact. Then, of course, there is the possibility that the oxynitride was formed as this phase has on occasional been suspected during other ambient atmosphere graphite die hot pressing and forging experiments.

The solution to the preform problem was to isostatically press and shape a preform as described above. The shaped specimen was then sintered in either a H_2 or air furnace under the minimum thermal cycle needed to achieve about 23% density. The cycle was chosen so the grain size would remain in the 1-3 μm range for ease of forging.

During the course of the preform experiments and one intermediate forging (No. 1456), the specimen liquified. It was suspected that free B_2O_3 in the BN was reacting with Al_2O_3 leading to experiments with various grades of BN and purified BN. When this did not solve the problem, a careful analysis of the true die cavity temperature was conducted. During the course of the run, temperature calibration experiments were carried out with auxiliary pyrometers and cleaning the mirror used in sighting into the cavity. After the run was complete, the sight tube window was removed and checked for absorption by sighting into the cavity. After the run was complete, the sight tube window was removed and checked for absorption by sighting into a constant temperature source. All of the errors led toward underestimating the true temperature and the following corrections were identified for operating at 1860°C; difference between pyrometers (both within calibration) - 20-25°C, mirror absorption - 17°C, condensation film on mirror - 15-20°C, window absorption - 17°C, film on outside of sight tube - 10°C, film on inside of sight tube - 5°C, difference between sight hole in die and cavity - 20-25°C. Thus, just these errors alone account for a possible 115°C error and the potential exists for other errors such as effects due to convection. The experiments demonstrated that temperature > 1975°C may have been realized in some of the experiments and this is above the MgAl_2O_4 - Al_2O_3 eutectic (1940°C) and could well approach the melting point of Al_2O_3 (2040°C). The question remains as to the effect of a B_2O_3 impurity in the BN, but it is certain that eutectic reactions are possible at these excessively high temperatures. The last forging experiments accounted for the additive effect of temperature measurement errors. All temperatures reported in Tables IV and V account for the possible errors above except for possible differences between pyrometers and adsorption by a film on the outside of the sight tube (a 65°C additive correction was made).

The final three forgings were conducted using the high strength Poco graphite fixture. During these runs the back-up punches limited the maximum pressure pressure to ~ 8000 psi as demonstrated by the failure of the system at 8300 psi during run 1497.

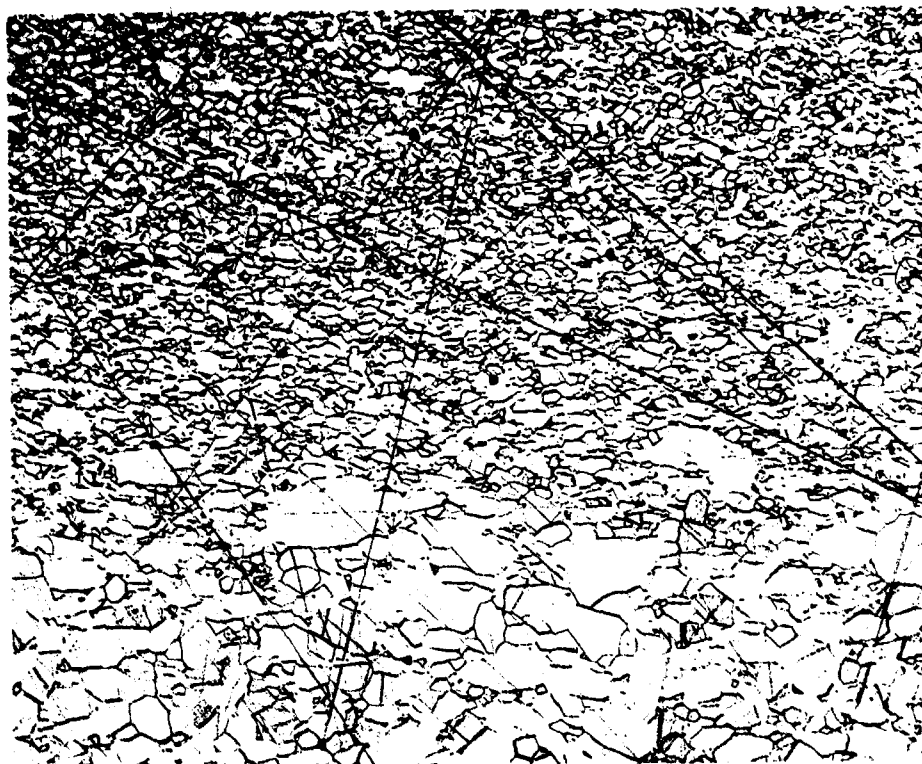
Forging 1486 resulted in a hemisphere that was very translucent over about 2/3 of the surface area. The rim section was porous and cracked

and, of course, is responsible for the overall low measured density. The Poco die was constructed so that this zone might be eliminated by the application of back pressure if the forging can be extended slightly beyond the full hemisphere (see Figure 20). A microstructural examination of the central translucent zone established that it was single phase and free of BN intrusions. The microstructure was not uniform through the cross section. Near the convex surface the structure was more pore free than on the concave surface and the structure was large grain size (33 μ m grain intercept) and equiaxed as compared with the oriented fine grain size (12 μ m grain intercept) toward the middle and concave side. These features are illustrated in Figure 25.

Forging 1493 was conducted with an 80 gram preform as compared with 50 grams for 1486. This insured a greater height reduction and also provided more material in an attempt to achieve the back pressure condition referred to above. The forging pressure was also increased 1300 psi, but this did not improve the lateral forging (the piece ended up thicker than 1496). This sample was also quite translucent in the central zone and is illustrated in Figure 26. A second phase was apparent (Figure 27) in the finer-grained section near the concave surface. Also, one area near surface the exhibited porosity entrapped within grains (Figure 28). This of course, is highly undesirable with regard to achieving transparency. It is suspected that both the second phase and the entrapped porosity problem are associated with the use of die lubricants. The fact that they were highly localized lends support for their eventual elimination. Figure 29 illustrates the surface to surface microstructure of this hemisphere. The large grain size surface regions may be due to impurities from the lubricants. Only one zone of microstructural texture was observed while the entire center of the section is fine grained and equiaxed. One region of mixed grain size strongly suggests recrystallization, but it is not possible to say whether or not the fine grain center represents a recrystallized zone. Of course, the strong microstructural texture is indicative of a highly deformed unrecrystallized area.

Both 1486 and 1493 forgings stuck to one part of the punch assembly. In part, this was caused by experimental difficulty in hot extracting the male punch. The different coefficients of expansion for the various grades of graphite caused binding that inhibited this step. Chemical reactivity may have been responsible for some of the sticking, particularly in the second forging where residue remained after forging 1486. Microcracks were observed in both forgings and were attributed to the sticking problem.

The premature termination of forging 1497 provided an opportunity to examine an intermediate stage in the microstructural development. The porosity and grain size gradient was quite pronounced as shown in Figure 30, a and b. Also, a second phase identical in appearance to Figure 27 was observed in the more porous zone adjacent to the concave surface. This sample was not contracted onto a punch and was free of any microcracks. The incomplete lateral forging may have contributed to the lack of binding. The microstructure evaluation showed that the concave surface densifies first. The porous outer zone representing about 2/3 of the section to the convex surface possessed an equiaxed grain structure. Presumably porosity



#5409-3

100X

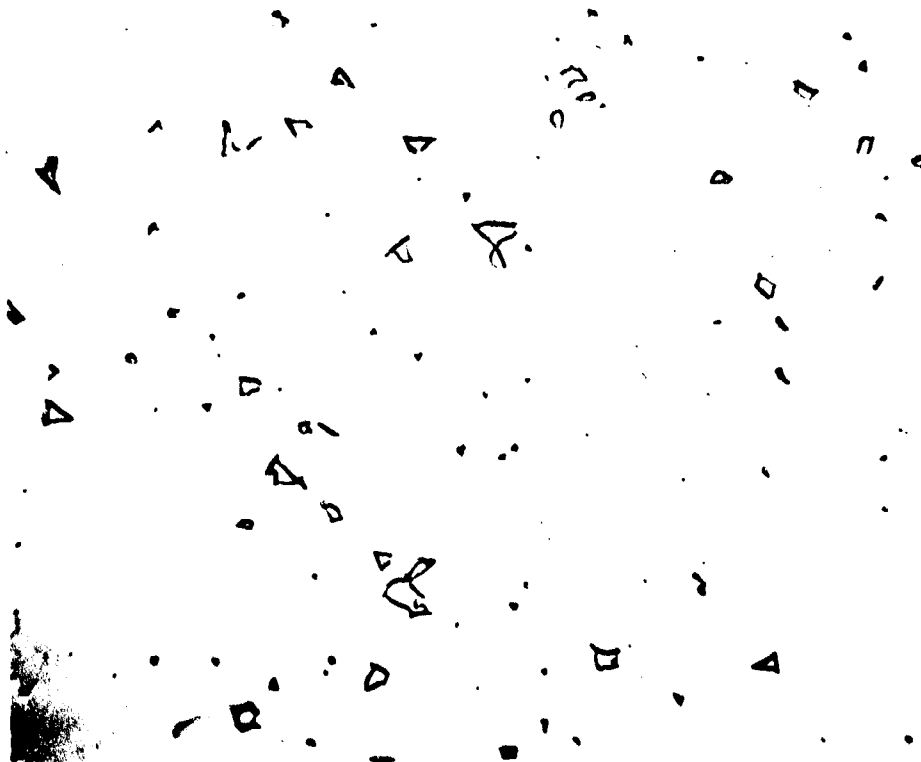
Figure 25. Cross-Section of Hemispherical Forging 1486
Showing Large-Grained Transparent Area and
Textured Slightly Porous Area.



#5300-3

1 1/2X

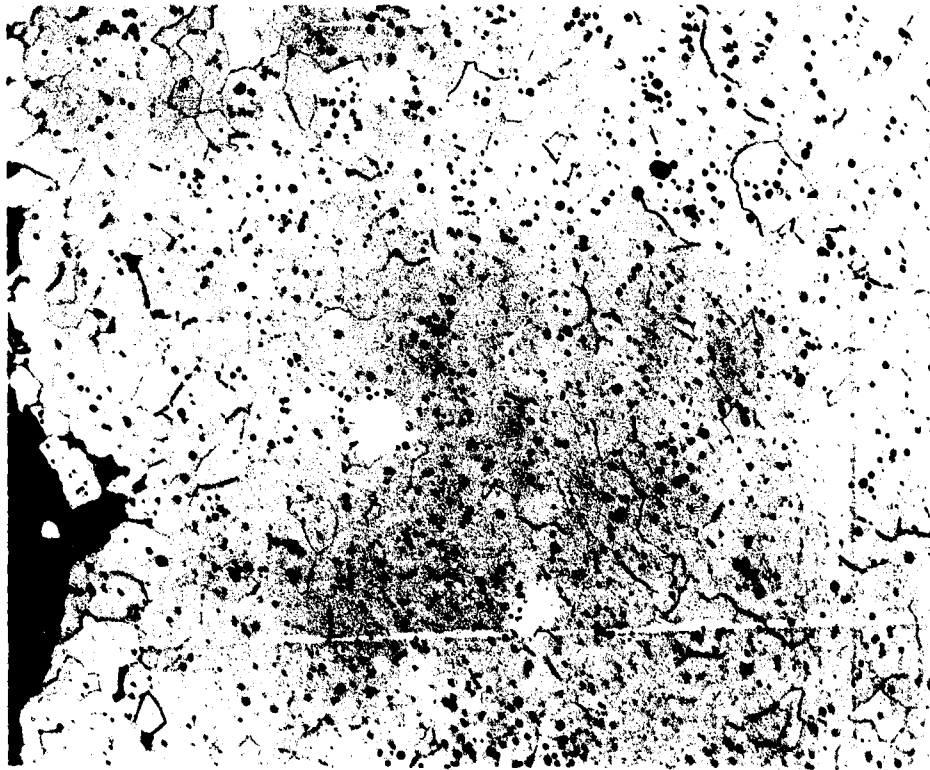
Figure 26. Section of Press Forged Alumina Hemisphere 1493.



#5448-8

500X

Figure 27. Second Phase Found Near Surface in One Local Area of Hemisphere 1493.



#5448-7

100X

Figure 28. Entrapped Porosity Near One Edge Surface of Hemisphere 1493.

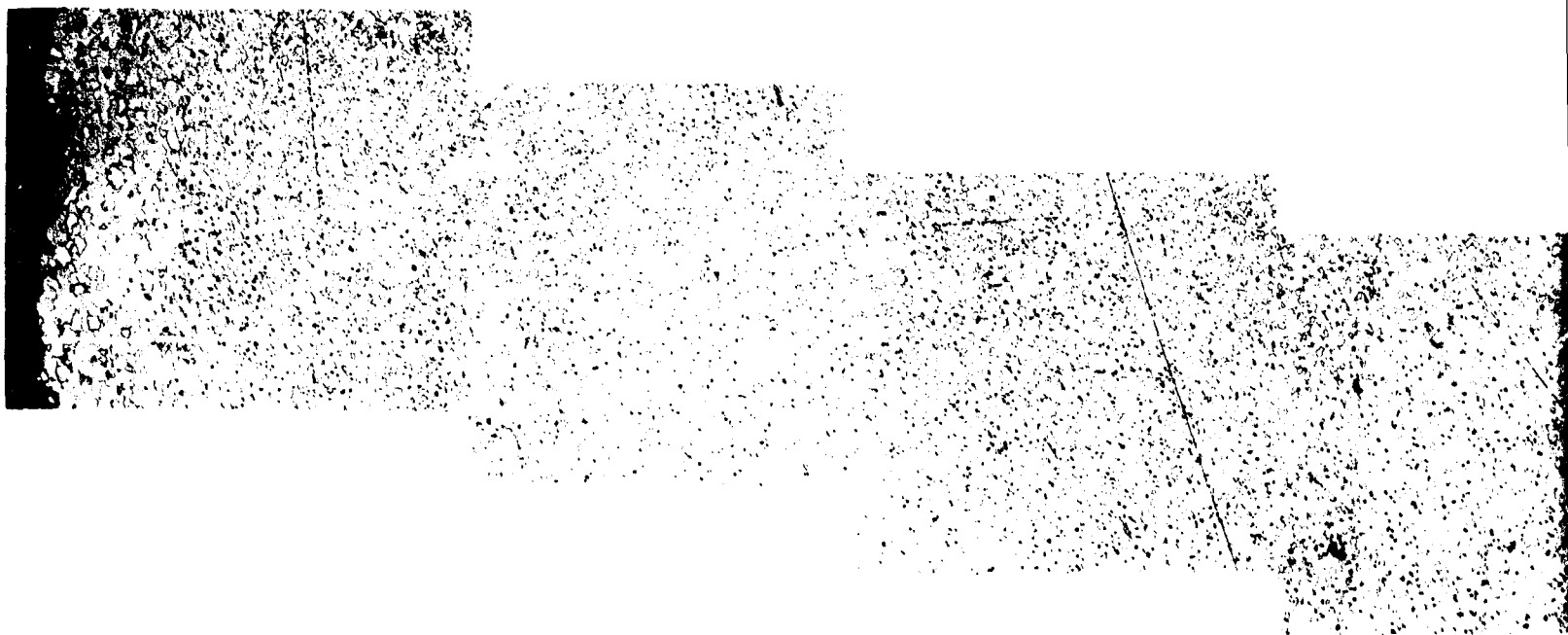
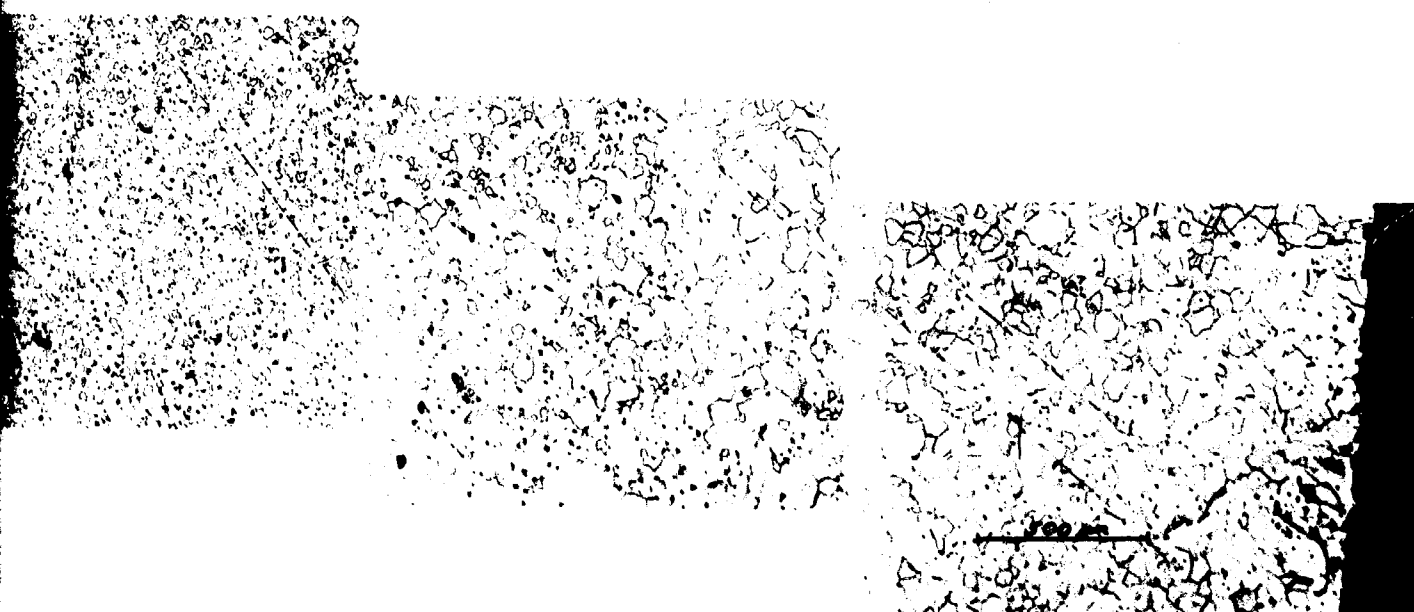


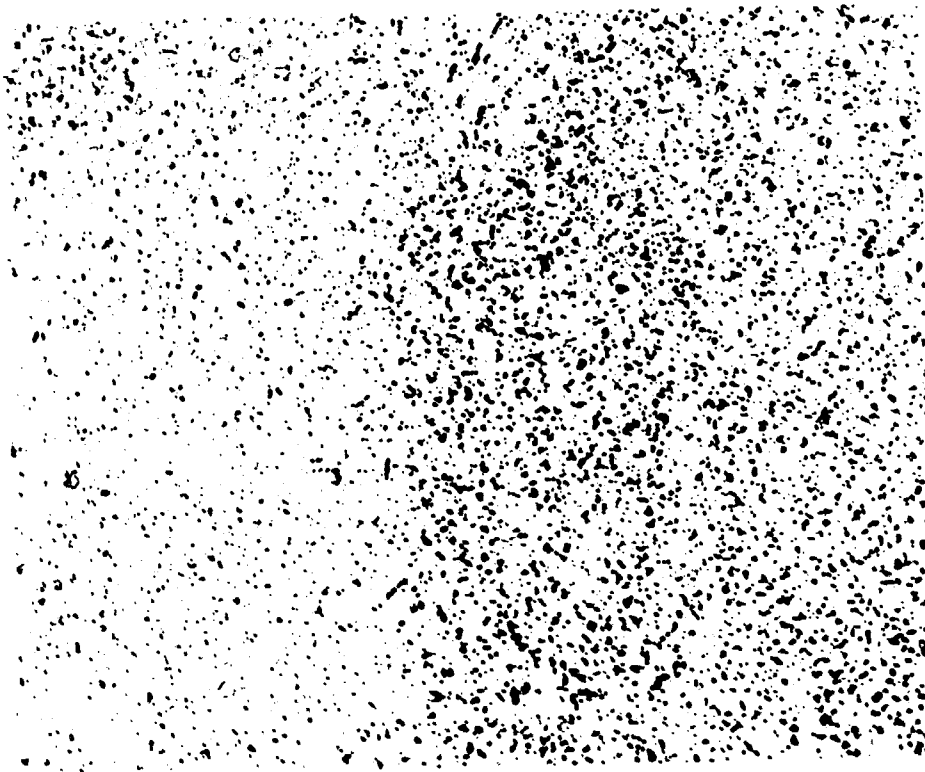
Figure 29. Microstructure of Entire Cross-Section of

Q



ire Cross-Section of Hemisphere 1493.

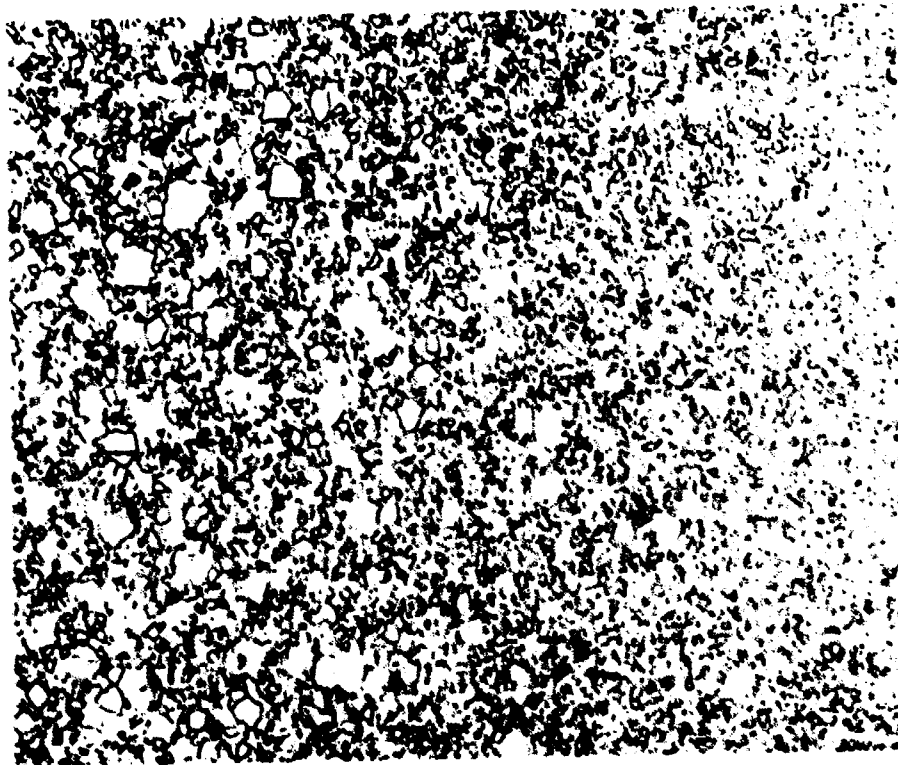
B



#5448-1

(a)

100X



#5448-3A

(b)

100X

Figure 30. Microstructure of Hemisphere 1497 Interrupted in Forging Showing, (a) Porosity Gradient and, (b) Grain Size Gradient.

restricted grain growth to some degree while the dense zone was free to undergo normal and some secondary growth. This type of stepped microstructure evolution may have been responsible for the duplex zone noted in Figure 29.

The thickness profiles for a number of the forgings are plotted in Figure 31. Examination of the profiles for Nos. 1497 and 1493 both from 80 gram preforms illustrates an intermediate and final cross-sectional variation, respectively. As expected the thick region is at the apex, the region from which the material flowed. The discontinuity in the slope of the 1493 (1486) profile occurs at about the preform diameter. Thus, it could be caused by a buckling in initial deformation or high surface friction. The lack of discontinuity in several hemispheres suggests that the problem has a solution, and, the fact that it is not as apparent in the 1497 (short) run strongly suggests that the effect is caused by friction. The 1493 profile shows that continued forging results in additional material flow outward from the apex without substantial thickening increase in the cross-sectional thickness. Presumably the wall would thicken once the outer limit of the die was reached and back pressure was applied. This condition would lead to a more uniform thickness as well. Alteration of the deformation parameters as well as more efficient lubricants should lend aid in thickness control.

An inverse pole figure x-ray study was conducted on Specimen 1432. Sections near the apex and the rim were examined with the results shown in Figure 32. The preferred crystallograph orientation was for the basal plane to be oriented normal to the surface of the specimen which for the rim section meant that the basal planes were oriented nearly normal to the direction of pressure application. These results indicate that the flow of material is in large part due to basal slip which, of course, conforms to the findings on upset forgings on discs. The R intercept value for the basal plane was 5 as compared with values as high as 51, but more usually 5-20 for disc forgings. Thus, the preferred crystallographic orientation was on the low end of that achieved in the disc forging effort.

The work to date demonstrates that Al_2O_3 hemispheres with a moderate degree of crystallographic orientation can be forged. Techniques for fabricating sound preforms have been largely solved. The last few forgings looked extremely promising in terms of producing hemispheres free of cracks for 140° of arc. The elimination of rim cracking will require one or a combination of the following; development of back pressure earlier in the forging cycle, shaped preforms or improved die lubricants. Forging 1486 was completely free of second phase, so this problem which has cropped up in several forgings certainly can be solved. Perhaps the most difficult problem will be the elimination of porosity. The convex surface of several forgings looked extremely pore-free and equivalent to the best disc forgings. It appears that this area receives the highest tensile strain and undergoes primary recrystallization while the zone near the male punch does not receive enough strain to recrystallize. It is thought that the recrystallized zone can be extended by increasing strain rate, increasing total strain (taller preforms), or forging at lower temperatures where recovery occurs less rapidly. The degree of the preferred orientation should vary with some of the experiments already mentioned and it is desirable to have high orientations for improved in-line transmission.

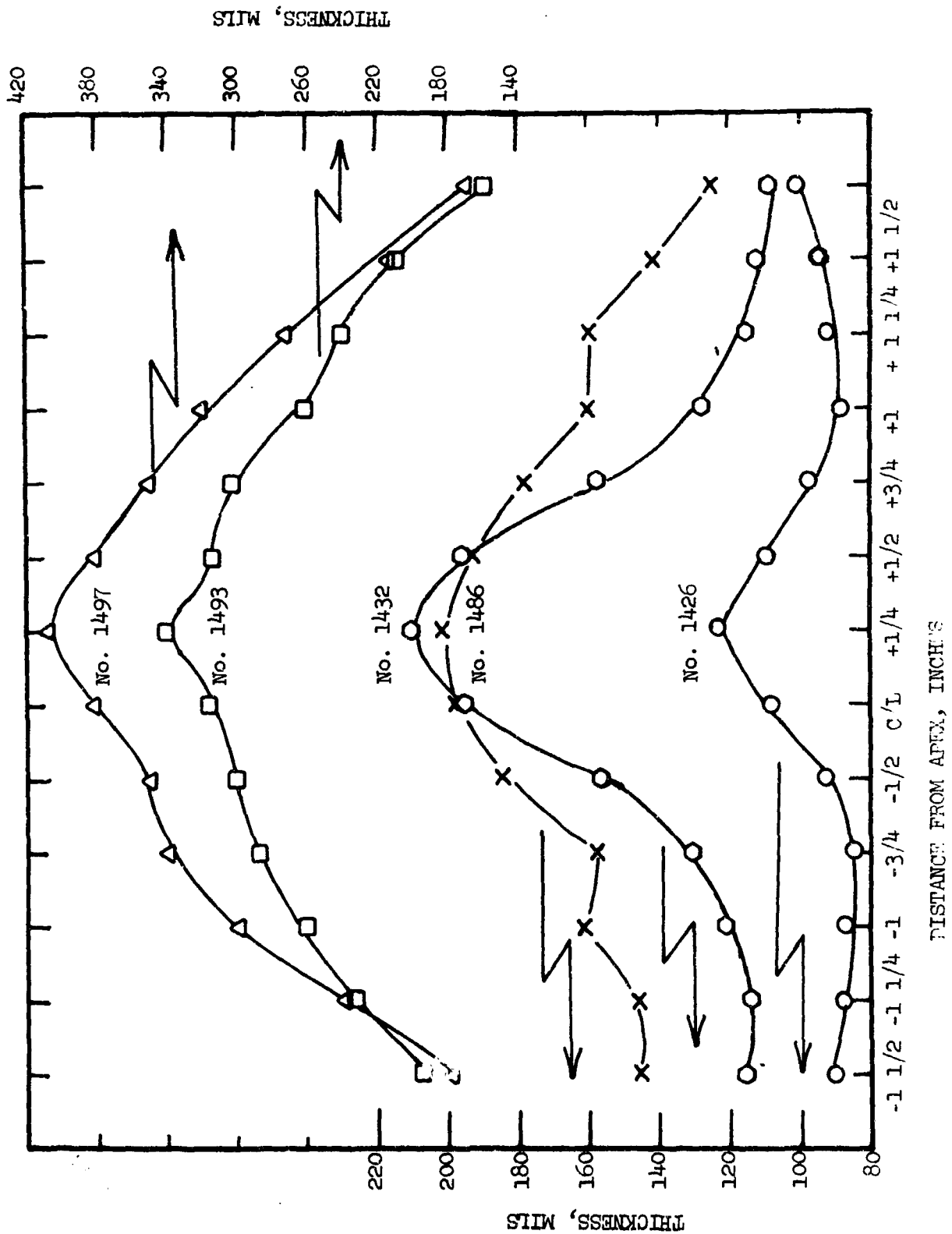
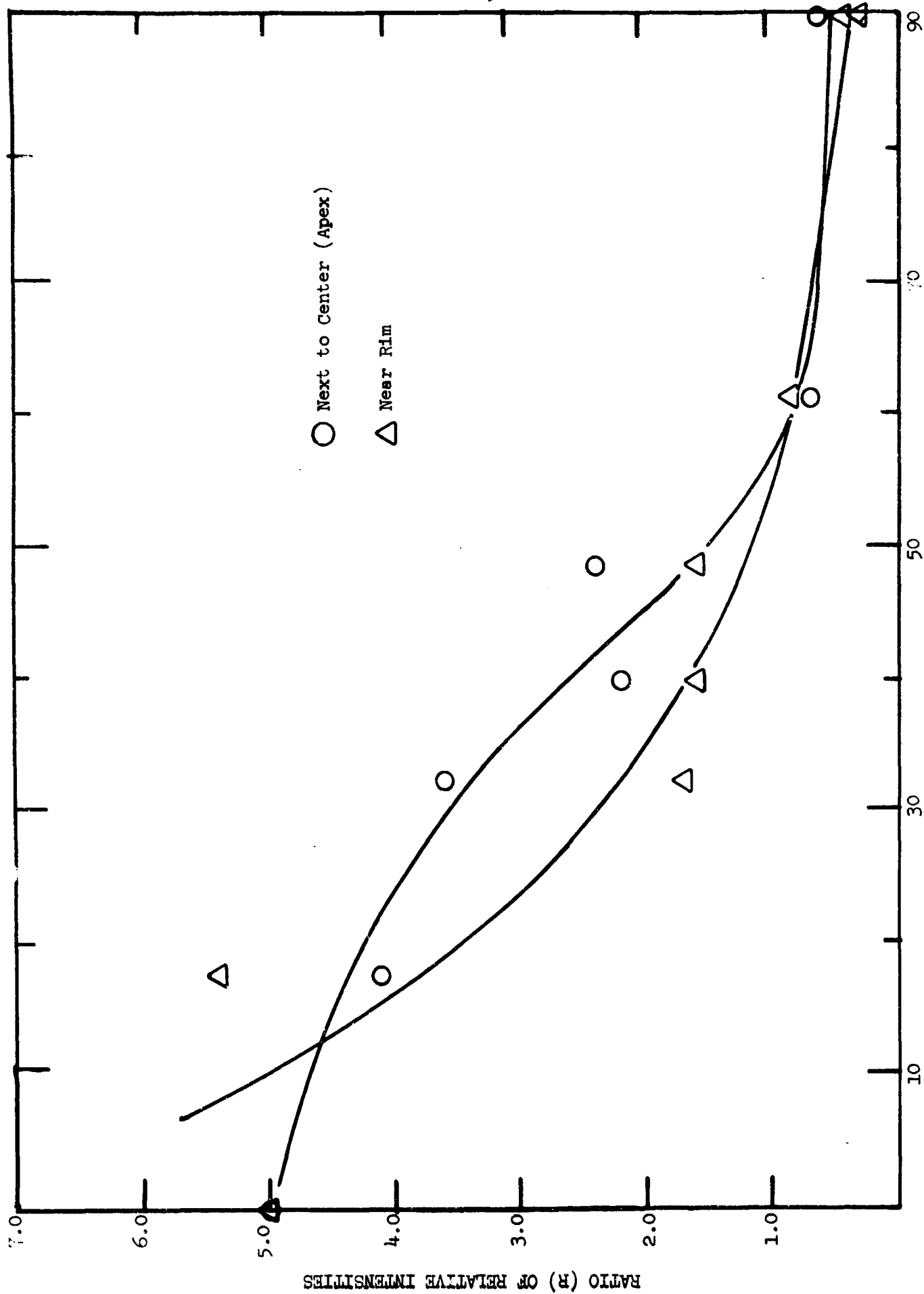


Figure 31. Thickness Profiles for Press Formed Al_2O_3 misp. eres.



ANGLE (ϕ) FROM BASAL PLANE

Figure 32. Ratio of Relative X-ray Intensities for Center and Rim of Hemisphere 1432.

Higher total strain, raising strain rate and lowering forging temperature are variables which should favor stronger orientations. Of course, there are some very real parameter constraints such as the strength of the graphite, the onset of cavitation within the specimen and the development of macroscopic cracking.

D. Summary

1. Alumina hemispheres were press-forged from powder and presintered preforms which were highly translucent over 140° arc.
2. A preferred basal crystallographic texture was developed parallel to the hemisphere surface which was attributed to basal slip playing a strong role in the deformation process.
3. A strong microstructural texture was observed near the concave surface with associated porosity while the convex surface was significantly more pore free, equiaxed and of a larger grain size suggesting a primary recrystallized grain structure at this surface.
4. Preform cracking, second phase development, melting, density gradients, agglomerate microcracks are all problems that were encountered and largely solved.
5. The problem areas remaining to be solved are complete pore removal, improving the crystallographic texture, and elimination of rim cracks.

V. REFERENCES

1. Oishi and W.D. Kingery, J. Chem. Phys., 33, 480 (1960).
2. A.H. Heuer, R.M. Cannon, and N.J. Tighe, "Plastic Deformation of Fine-Grained Ceramics," in Ultra-Fine Grain Ceramics, Syracuse University Press.
3. R.M. Cannon and W.H. Rhodes, "Deformation Processes in Forging Ceramics," Contract NASW-1914 (August 1970).
4. O.D. Sherby, Acta. Met., 10, 135 (1962).
5. R. Vandervoort, Trans. AIME, 242, 345 (1968).
6. D. Holt and W. Backofen, Trans. AIME, 242, 345 (1968).
7. C. Herring, J. Appl. Phys., 21, 437 (1950).
8. R.H. Coble, J. Appl. Phys., 34, 1679 (1963).
9. R.C. Gifkins, J. Am. Ceram. Soc., 51, 69 (1968).
10. R.N. Stevens, Meta. Rev., 11, 129 (1966).
11. W.H. Rhodes and R.M. Cannon, "Microstructure Studies of Refractory Polycrystalline Oxides," Contract N00019-69-C-0198, December 1969.
12. W.H. Rhodes, P.F. Jahn, P.L. Burnett, "Microstructure Studies of Refractory Polycrystalline Oxides," Contract N00019-68-C-0108, June 1969.
13. W.H. Rhodes, D.J. Sellers, R.M. Cannon, A.H. Heuer, W.R. Mitchell, and P.L. Burnett, "Microstructure Studies of Polycrystalline Refractory Oxides," Contract N00019-67-C-0336, Summary, 1968.
14. S. Timoshenko, Strength of Materials, Part II, 3rd edition, D. Van Nostrand, Princeton, p. 527 (1956).
15. R.M. Cannon and A.H. Heuer, to be published.
16. R.M. Spriggs, J.B. Mitchell and T. Vasilos, J. Am. Ceram. Soc., 47, 323 (1964).
17. P.J. Jorgensen, J. Am. Ceram. Soc., 48, 207 (1965).
18. R.C. Folweiler, J. Appl. Phys., 32, 773 (1961).
19. S.I. Warshaw and F.H. Norton, J. Am. Ceram. Soc., 45, 479 (1962).
20. E.M. Passmore and T. Vasilos, J. Am. Ceram. Soc., 49, 166 (1966).

V. REFERENCES (Cont'd)

21. R.E. Mistler, "Grain Boundary Diffusion and Boundary Migration Kinetics in Aluminum Oxide, Sodium Chloride and Silver," Sc.D. Thesis, Mass. Inst. of Technology, 1967.
22. D.L. Johnson and L. Berrin, "Grain Boundary Diffusion in the Sintering of Oxides," in Sintering and Related Phenomena, edited by G.C. Kuczynski, N.A. Hooton and C.G. Gibbon, Gordon and Breach, Science Publishers, New York (1967).
23. R. Chang, "Diffusion Controlled Deformation and Shape Change in Non-Fissionable Ceramics," in Proceedings of the Conference on Nuclear Applications of Non-Fissionable Ceramics, ed. A. Boltax and J.H. Handwerk, American Nuclear Society (1966).
24. F.J.P. Clarke, R.A.J. Sambell and H.G. Tattersall, Phil. Mag., 1, 393 (1962).
25. A.R. Westwood, D.L. Goldheim and R.G. Lve, Phil. Mag., 16, 505 (1967).
26. A.R.C. Westwood and R.M. Latanision, "Environment-Sensitive Machining Behavior of Non-metals," Contract No. N00014-70-C-0330, October 1970.
27. R.W. Rice, J.G. Hunt, G.I. Freedman and J.L. Sliney, "Identifying Optimum Parameters of Hot Extrusions," Contract NAS7-276.
28. M.H. Leipold and T.H. Nielsen, Bull. Am. Ceram. Soc., 45, (3), 281-85 (1966).
29. W.H. Rhodes, B.J. Wuensch, and T. Vasilos, "Relation Between Particulate Chemistry and Ceramic Properties," Contract N00014-70-C-0138.
30. W.B. Harrison, Honeywell, private communication.
31. S.M. Copley and J.A. Pask, J. Am. Ceram. Soc., 48, 636 (1965).
32. W.B. Harrison, J. Am. Ceram. Soc., 47, 574 (1964).
33. D.J. Sellers, A.H. Heuer, W.H. Rhodes and T. Vasilos, J. Am. Ceram. Soc., 50, 217 (1967).
34. W.H. Rhodes, D.J. Sellers, A.H. Heuer and T. Vasilos, "Development and Evaluation of Transparent Aluminum Oxide," N178-8986, Final Report June 1967.
35. A.H. Heuer, D.J. Sellers and W.H. Rhodes, J. Am. Ceram. Soc., 9, 468 (1969).

V. REFERENCES (Concl'd)

36. A.H. Heuer, W.H. Rhodes, D.J. Sellers and T. Vasilos, "Micro-structure Studies of Polycrystalline Refractory Oxides," NOW-66-0506(d), Summary Report (1967).
37. R.M. Haag, "Magnetic-Crystallographic Orientation Produced in Ferrites by Hot Working," Contract N00014-68-C-0364.
38. S.K. Roy and R.L. Coble, J. Am. Ceram. Soc., 50, 435 (1967).